

# Two-Dimensional Silver(I)-Dithiocarboxylate Coordination Polymer Exhibiting Strong Near-Infrared Photothermal Effect

Mu-Qing Li,<sup>†,‡</sup> Min Zhao,<sup>†</sup> Le-Yu Bi,<sup>†</sup> Yue-Qiao Hu,<sup>†,§</sup> Gaoyang Gou,<sup>\*,†</sup> Ju Li,<sup>\*,†,||</sup> and Yan-Zhen Zheng<sup>\*,†</sup>

<sup>†</sup>Frontier Institute of Science and Technology (FIST), State Key Laboratory of Mechanical Behavior for Materials, MOE Key Laboratory for Nonequilibrium Synthesis of Condensed Matter, Xi'an Key Laboratory of Sustainable Energy and Materials Chemistry and School of Science, Xi'an Jiaotong University, 99 Yanxiang Road, Xi'an, Shaanxi 710054, People's Republic of China

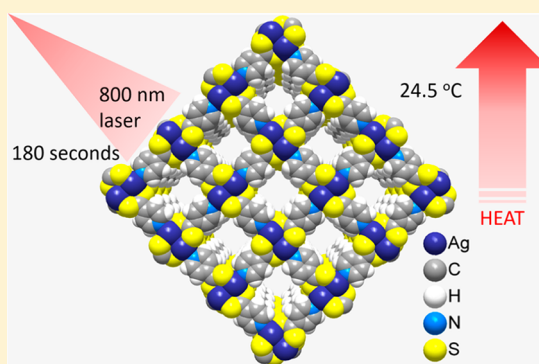
<sup>‡</sup>Department of Chemistry, City University of Hong Kong, 83 Tat Chee Avenue, Kowloon, Hong Kong, China

<sup>§</sup>Key Laboratory of Advanced Molecular Engineering Materials, Baoji University of Arts and Sciences, No. 1 Hi-Tec Avenue, Baoji 721013, People's Republic of China

<sup>||</sup>Department of Nuclear Science and Engineering, Department of Materials Science and Engineering, Massachusetts Institute of Technology, Cambridge, Massachusetts 02139, United States

## Supporting Information

**ABSTRACT:** Materials that demonstrate near-infrared (NIR) absorption and can simultaneously convert the electromagnetic irradiation into heat are promising for photothermal therapy. Traditionally, such a material is either pure inorganic, such as CuS, Ag<sub>2</sub>S, and carbon nanotube, or pure organic, such as polyaniline, polypyrrole, and conjugated polymers. Here we show that strong NIR photothermal effect can also be achieved in inorganic–organic hybrid coordination polymers (CPs) or metal–organic frameworks (MOFs). Our strategy is to construct CPs with inorganic Ag–S components that are interlinked by the organic ligands into a higher-dimensional hybrid network. Interestingly, the two resulting CPs, [Ag(Py-4-CSS)]<sub>n</sub> **1** and [Ag<sub>2</sub>(Py-4-CSS)(Py-4-CSSS)]<sub>n</sub> **2** (Py-4-CSS = pyridine-4-dithiocarboxylate; Py-4-CSSS = pyridine-4-perthiocarboxylate), show disparate structures due to the varied coordination mode of the pyridine group. For **1**, the N atom coordinates to the Ag<sup>+</sup> center and forms a two-dimensional square framework, while for **2**, such a Ag–N bond is disconnected and forms only a one-dimensional structure. Interestingly, this difference leads to the distinct absorption properties in the NIR region. Under 800 nm radiation, the temperature of **1** can rise up to 24.5 °C in 3 min with photothermal conversion efficiency of 22.1%, which is about 2× that of pure inorganic Ag<sub>2</sub>S material and among the highest compared to various known inorganic materials, for example, Au nanoshells (13%), nanorods (21%), and Cu<sub>2-x</sub>Se nanocrystals (22%) irradiated with 800 nm light, while for **2**, the NIR absorption is absent. This result first demonstrates that the inorganic–organic hybrid approach can be applied to construct superior NIR photothermal materials, but the control of the structure is vital. Here the coordinating nitrogen atoms in **1** are conceived to be critical in promoting the charge transfer between the dithiocarboxylate ligands. To elucidate the response to NIR irradiation of **1**, we measured the heat capacity and dielectric constant of **1** and also performed density functional theory calculations. Significantly, the large dielectric constant and flat energy bands indicates **1** is much easier to be polarized and has a high electron effective mass. Thus, unlike the pure inorganic material, such as Ag<sub>2</sub>S, in which electron and hole can quantum mechanically combine to give off light, the joint-force of organic ligands in **1** effectively enhances polaronic recombination into heat.



## INTRODUCTION

Narrow band gap semiconductors that enable the conversion of electromagnetic irradiation to heat<sup>1</sup> in near-infrared (NIR) windows (750–850 nm NIR-I and 1000–1320 nm NIR-II) hold great promise in photothermal therapy.<sup>2–8</sup> Typical inorganic NIR semiconductors include CuS,<sup>9</sup> Ag<sub>2</sub>S,<sup>10</sup> and carbon nanotube,<sup>11</sup> while organic NIR semiconductors are represented by polyaniline,<sup>12</sup> polypyrrole,<sup>6,7</sup> and donor–acceptor (D–A) conjugated polymers.<sup>13</sup> In fact, inorganic and organic semiconductors show complementary advantages

in NIR photothermal application. For instance, the inorganic ones are thermally more stable, while the organic ones are easier to fold and extend. In addition to these properties, strong NIR absorbance, excellent photostability, rapid clearance,<sup>14</sup> and additional functions (e.g., imaging capability<sup>3</sup> and drug loading capability<sup>4</sup>) are also important targets of the design of NIR photothermal materials.

Received: October 9, 2018

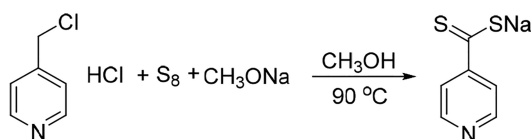
Published: April 30, 2019

Coordination polymers (CPs), also known as metal–organic frameworks (MOFs), are a class of inorganic–organic hybrid materials with designable features of both organic linkers and inorganic joints.<sup>15–17</sup> CPs have been widely investigated in various applications like gas adsorption, luminescence, and catalysis.<sup>18,19</sup> Recently, this class of materials have been used for photothermal therapy. As demonstrated by Liu and Wu, nanoscale MOF particles or sheets comprising photosensitizers are very efficient at generating a strong NIR photothermal effect,<sup>14,20</sup> but the main contribution of this effect is from the organic ligands. In this paper, we show another design of an efficient NIR photothermal converter by combining both contributions from inorganic and organic components. As Ag<sub>2</sub>S is a well-known inorganic semiconducting material for NIR photoluminescence<sup>21</sup> and photothermal effect,<sup>10</sup> we reason that the incorporation of effective Ag–S component into CPs with conjugated organic linkers is promising for the targeted materials.

However, to synthesize such a material is very challenging due to the strong reactivity between silver(I) and sulfide. Even the sulfur atom is part of the organic ligand it can be deprived of by the Ag(I) ions and forms silver sulfide instead. To prevent or delay such a reaction, previous efforts tried to use some “tamed” thiol ligands containing one thiol group and some electron-withdrawing function groups.<sup>22–25</sup> Though some CPs with Ag–S nodes, chains, and layers have been obtained by this method, such Ag–S-based CPs are of light colors,<sup>23</sup> indicating a large band gap and, thus, poor NIR absorption. The wide band gap was known to be the effect of quantum confinement owing to the small size of the Ag–S components in these CPs. Compared to thiol, the dithiocarboxylate group bearing the same charge but more sulfur atoms may form bigger Ag–S components. Some known silver dithiocarboxylate compounds do show relatively darker colors, indicating the ability of absorbing long wavelength irradiation.<sup>26–28</sup>

To achieve this goal, we synthesized a new dithiocarboxylate ligand, pyridine-4-dithiocarboxylate (Py-4-CSS<sup>−</sup>), using a sulfurization reaction of aromatic methyl halide (Scheme 1).<sup>29</sup> Reaction of sodium pyridine-4-dithiocarboxylate (Py-4-

**Scheme 1. Synthesis of Py-4-CSSNa**



CSSNa) and AgNO<sub>3</sub> in mixed methanol/water solution at low temperature produces a dark green crystalline solid product of [Ag(Py-4-CSS)]<sub>n</sub> **1** with high yield (Figure S3). Larger single crystals of **1** for X-ray diffraction analysis were selected by solvothermal treatment of Py-4-CSSNa and AgNO<sub>3</sub> in the presence of FeSO<sub>4</sub> and NaCl. Interestingly, some red crystals of [Ag<sub>2</sub>(Py-4-CSS)(Py-4-CSSS)]<sub>n</sub> **2** (Py-4-CSSS<sup>−</sup> = pyridine-4-perthiocarboxylate) appear along with **1** after the solvothermal reaction. The (−CSSS)<sup>−</sup> group formed from oxidative reaction of the dithiocarboxylate group has been observed previously.<sup>30,31</sup> Remarkably, **1** shows obvious absorption and exceptionally high photothermal response under NIR irradiation.

## EXPERIMENTAL SECTION

All reagents are commercially available and were used as received without further purification.

**Synthesis of Sodium Pyridine-4-dithiocarboxylate (Py-4-CSSNa).** Under an inert atmosphere, elemental sulfur (1.28 g, 40 mmol), sodium methoxide (3.24 g, 60 mmol), and methanol (100 mL) were added to a two-head flask charged with a stir bar, and the mixture was stirred for 3 h in 70 °C oil bath. After cooling down, 4-(chloromethyl)pyridine hydrochloride (3.28 g, 20 mmol) was added. The mixture was then stirred for 9 h in a 90 °C oil bath. Then methanol was removed from the resulting mixture under reduced pressure, leaving a yellow solid. Dry tetrahydrofuran (THF; 50 mL) was added to dissolve the yellow solid, and the mixture was filtered with cannula capped with filter paper under nitrogen. Orange solid (2.48 g, 70% yield) was left after THF being removed from the filtrate under reduced pressure, and the product was used without further purification. Elemental analysis found C 40.21%, H 3.02%, N 7.47%, S 32.06%, matching the formula C<sub>6</sub>H<sub>4</sub>NS<sub>2</sub>Na(THF)<sub>0.2</sub>(H<sub>2</sub>O)<sub>0.4</sub> (calcd: C 40.44%, H 3.09%, N 7.15%, S 32.71%). <sup>1</sup>H NMR (400 MHz, MeOD-*d*<sub>4</sub>): δ 8.36 (m, 2H), 7.83 (m, 2H). <sup>13</sup>C NMR (100 MHz, MeOD-*d*<sub>4</sub>): δ 121.80, 149.03, 162.65.

**Synthesis of Single Crystals of **1** and **2**.** Single crystals of **1** and **2** suitable for single crystal X-ray diffraction were obtained by a solvothermal reaction under an inert atmosphere: FeSO<sub>4</sub>·7H<sub>2</sub>O (28 mg) and Py-4-CSSNa (18 mg) were mixed in DMF (2 mL) and acetonitrile (1 mL), while silver nitrate (17 mg) and sodium chloride (20 mg) were mixed in DMF (1 mL). The two suspensions were mixed in a vial and cap sealed. The vial was heated in an oven at 80 °C for 2 days. After cooling down, several black crystals of **1** and red crystals of **2** were isolated. With this method, we obtained big crystals of **1** just once, and most of the time, we obtained crystals of **2** only, and the characterizations of **2** were carried out with the single crystals isolated.

**Synthesis of Polycrystalline **1**.** Crystalline powder sample of **1** was synthesized by direct mixing aqueous solution of AgNO<sub>3</sub> and methanol solution of Py-4-CSSNa in low temperature (ice bath). Py-4-CSSNa (354 mg, 2 mmol) was dissolved in methanol under N<sub>2</sub>. The solution was added to an aqueous solution of AgNO<sub>3</sub> (340 mg, 2 mmol in 50 mL of degassed water) in an ice bath under N<sub>2</sub>. Dark green precipitate appeared immediately. The mixture was stirred for 2 h and the solid was isolated by filtration. The solid was washed with water and THF and then dried under N<sub>2</sub> (419 mg). Powder XRD of the crystalline sample of **1** matches well with that calculated from the structure got by single crystal XRD analysis indicating the same structure and pure phase of the crystalline sample (Figure S5). Elemental analysis result of the powder (C 27.14%, H 1.90%, N 4.69%, S 22.81%) is close to the calculated component for formula C<sub>6</sub>H<sub>4</sub>NS<sub>2</sub>Ag(H<sub>2</sub>O)<sub>0.6</sub>(THF)<sub>0.1</sub> (C 27.44%, H 2.16%, N 5.00%, S 22.89%).

**Synthesis of Polycrystalline **2**.** Under an inert atmosphere, Py-4-CSSNa (36 mg, 0.2 mmol), elemental sulfur (4 mg, 0.1 mmol), and acetonitrile (4 mL) were added to a glass vial charged with a stir bar, and the mixture was stirred for 3 h on a heating plate of 85 °C. After cooling down, an acetonitrile solution of AgNO<sub>3</sub> (34 mg, 0.2 mmol) was added. The mixture was then stirred for 12 h at room temperature, and the solid was isolated by filtration. The solid was washed with water and THF and then dried under vacuum (40 mg, yield 72%). Powder XRD of the crystalline sample matches well with that calculated from the structure got by single crystal XRD analysis of **2**, indicating the same structure and pure phase of the crystalline sample (Figure S6). Elemental analysis result of the powder (C 25.74%, H 1.50%, N 5.09%, S 29.01%) is close to the calculated component for formula C<sub>12</sub>H<sub>8</sub>N<sub>2</sub>S<sub>5</sub>Ag<sub>2</sub> (C 25.90%, H 1.45%, N 5.04%, S 28.82%).

**X-ray Crystallography.** Single-crystal X-ray diffraction data collection for **1** and **2** were conducted on a Bruker SMART APEX II CCD diffractometer (Mo, λ = 0.71073 Å) at 296.15 K. The structures were solved by direct methods and refined with a full-matrix least-squares technique within the SHELXTL program

package<sup>32</sup> and Olex2.<sup>33</sup> All nonhydrogen atoms were refined anisotropically. The hydrogen atoms were set in calculated positions and refined using the riding model. For **1**, attempts to locate and model the highly disordered solvent molecules in the pores were unsuccessful. Therefore, the SQUEEZE routine of PLATON<sup>34</sup> was used to remove the diffraction contribution from these solvents. For **1**,  $P4/ncc$ , empirical formula  $C_{24}H_{16}Ag_4N_4S_8$ , MW 1048.37,  $T = 296.15$  K,  $a = b = 16.125(3)$  Å,  $c = 7.2075(12)$  Å,  $\alpha = \beta = \gamma = 90^\circ$ ,  $V = 1874.1(8)$  Å<sup>3</sup>,  $Z = 2$ ,  $\rho = 1.858$  g·cm<sup>-3</sup>,  $\mu = 2.525$  mm<sup>-1</sup>,  $R_1 = 0.0306$  for  $I \geq 2\sigma(I)$ ,  $wR_2 = 0.0787$  for all data; for **2**,  $P2_1/n$ , empirical formula  $C_{24}H_{16}Ag_4N_4S_{10}$ , MW 1112.49,  $T = 296.15$  K,  $a = 11.861(5)$  Å,  $b = 7.723(3)$  Å,  $c = 33.601(15)$  Å,  $\alpha = 90^\circ$ ,  $\beta = 95.299(5)^\circ$ ,  $\gamma = 90^\circ$ ,  $V = 3065(2)$  Å<sup>3</sup>,  $Z = 4$ ,  $\rho = 2.411$  g·cm<sup>-3</sup>,  $\mu = 3.227$  mm<sup>-1</sup>,  $R_1 = 0.0626$  for  $I \geq 2\sigma(I)$ ,  $wR_2 = 0.1238$  for all data. The crystallographic details are provided in Table S1. Selected bond distances and bond angles are listed in Tables S2 and S3. Crystallographic data for the structural analyses have been deposited at the Cambridge Crystallographic Data Center. CCDC reference numbers: 1819424 and 1821603. The crystallographic data for above compounds can be found in the Supporting Information or can be obtained free of charge from the Cambridge Crystallographic Data Centre via [http://www.ccdc.cam.ac.uk/data\\_request/cif](http://www.ccdc.cam.ac.uk/data_request/cif).

**Powder X-ray Diffraction (PXRD).** PXRD data were collected in the reflection mode at room temperature on a Bruker D8 Advanced X-ray diffractometer using Cu K $\alpha$  ( $\lambda = 1.5418$  Å) radiation. The X-ray tube operated at a voltage of 40 kV and a current of 40 mA.

**Fourier-Transform Infrared (FT-IR) Spectroscopy.** FT-IR spectra were obtained using a Nicolet 6700 FT-IR spectrophotometer with Smart iTR Attenuated Total Reflectance (ATR) Sampling Accessory.

**Raman Spectroscopy.** Raman spectra were recorded on a Horiba LabRAM HR Evolution Raman microscope with a laser of 785 nm.

**Nuclear Magnetic Resonance (NMR) Spectroscopy.** Solution <sup>1</sup>H NMR spectra were recorded on a 400 MHz Bruker superconducting magnet high-field NMR spectrometer at room temperature.

**Thermogravimetric Analyses (TGA).** TGA measurements were carried out in a flow of nitrogen using a Mettler Toledo TGA with a heating rate of 10 °C/min. The curve of **1** shows 6.6% weight loss before 232 °C, indicating a little solvent in the solid. The curve of **2** shows no obvious weight loss before 214 °C, corresponding to the solvent-free structure revealed by the single crystal X-ray diffraction.

**UV–vis-NIR Diffuse Reflectance Spectra.** UV–vis-NIR diffuse reflectance spectra were recorded with a Shimadzu UV-3600 UV–vis-NIR spectrophotometer equipped with an integrating sphere. The reflectance versus wavelength data generated were used to estimate the band gap of the material by transforming reflectance to absorption data according to the Kubelka–Munk equation:  $\alpha/S = (1 - R)^2/(2R)^{-1}$ , where  $R$  is the reflectance and  $\alpha$  and  $S$  are the absorption and scattering coefficients, respectively.

**Transmission Electron Microscopy.** Transmission electron microscopy (TEM) studies were conducted on a Hitachi HT-7700 transmission electron microscope with an accelerating voltage of 100 kV.

**Elemental Analysis.** C, H, N, and S analysis was conducted on an Elementar vario MACRO cube analyzer.

**Photothermal Effect.** Samples of **1** and Ag<sub>2</sub>S (250 mg) were pressed into dense discs of 13 mm diameter with 100 kN normal force. The samples are loaded on a white paper and the temperature was measured with a Fluke Visual IR Thermometer. 800 nm laser with power density of 0.754 W cm<sup>-2</sup> was generated with an infrared diode laser at 800 nm (MDL-III-800–2.5W from Changchun New Industries Optoelectronics Tech Co., Ltd.).

**Differential Scanning Calorimetry (DSC).** DSC measurement of **1** and Ag<sub>2</sub>S from 20 to 80 °C was performed in a Q200 Differential Scanning Calorimeter from TA Instruments. Specific heat capacity ( $C_p$ , J/(g·K)) was calculated from the DSC data.

**Dielectric Measurement.** Dielectric constant measurement was performed on a HIOKI 3532–50 LCR HiTESTER. Powder sample of **1** was pressed into a dense disc of 10 mm diameter and 0.9 mm

height. Silver paste was used to connect the pellet sample to the electrode probes.

**First-Principles Calculations.** We perform first-principles calculations based on density functional theory (DFT) implemented in the Vienna Ab Initio Simulation Package (VASP),<sup>35,36</sup> using projector augmented wave (PAW) pseudopotentials<sup>37</sup> and a plane wave basis set with an energy cutoff of 500 eV. We choose the strongly constrained and appropriately normed (SCAN)<sup>38</sup> meta-GGA functional<sup>39</sup> for structural optimization and electronic structure calculations. The  $10 \times 6 \times 6$  and  $4 \times 4 \times 8$  Monkhorst–Pack  $k$ -point grids<sup>40</sup> are used to sample the Brillouin zone for bulk  $\alpha$ -Ag<sub>2</sub>S and coordination polymer [Ag(Py-4-CSS)]<sub>n</sub> **1**, respectively. All atomic structures are fully relaxed until the Hellmann–Feynman force on each atom is less than 1 meV/Å and residual stress less than 0.1 kbar.

## RESULTS AND DISCUSSIONS

**Crystal Structures.** Single crystal X-ray diffraction analysis revealed **1** features a layered structure (Figure 1). Each

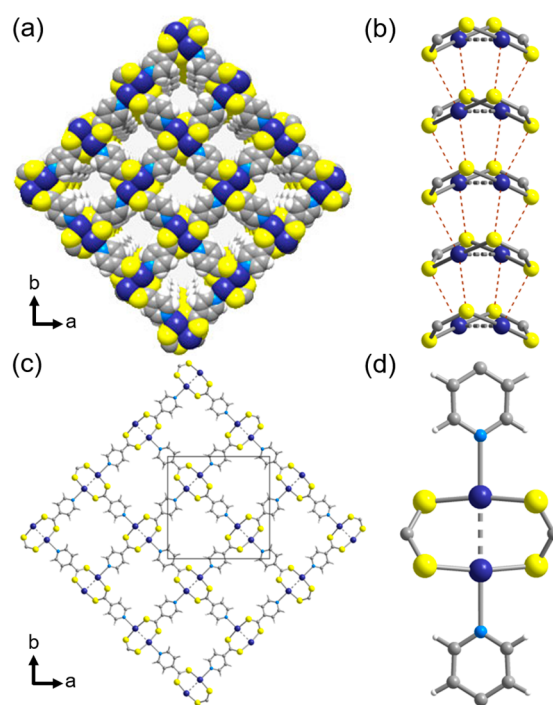


**Figure 1.** Packing diagram (a), interlayer Ag...S interactions (b), the single layer (c), and the SBU (d) of **1**. Color codes: silver, dark blue; sulfur, yellow; nitrogen, light blue; carbon, gray; hydrogen, white.

silver(I) ion coordinates two sulfur atoms and one nitrogen atom to generate a “T” shape [AgS<sub>2</sub>N] fragment. The Ag–S bond length (2.43 Å) and Ag–N bond length (2.53 Å) are in the normal range.<sup>28</sup> The distance of the two silver ions in the dimer is 3.04 Å, much shorter than twice of the van der Waals diameter (3.44 Å) of silver atom and close to the bond length in silver metal (2.89 Å). The short Ag...Ag distance indicates argentophilicity<sup>41</sup> in the dimers, which are bridged by four Py-4-CSS<sup>-</sup> ligands in the  $ab$  plane to construct a [4,4] square network.

The [Ag(Py-4-CSS)]<sub>n</sub> layers stack in a ABAB relation along  $c$  axis, leaving one-dimensional (1D) cylindrical pores with a van der Waals diameter of  $\sim 5$  Å. Interestingly, between neighboring layers, there are extensive Ag...S weak interactions (with distances shorter than 3.3 Å), which connect the [AgS<sub>2</sub>]<sub>2</sub>



dimers into a novel  $[\text{Ag}_2\text{S}_4]_n$  chain (Figure 1b). Pyridine rings between adjacent layers stack in a head-to-tail fashion along the  $c$  axis. The centroid...centroid contacts between the pyridine rings are about 3.64 Å, while displacement angles are around 28.4° (Figure S4). Such orientations of the aromatic rings indicate proper  $\pi$ - $\pi$  interactions between the layers, which may significantly contribute to the interlayer charge transport and thus affect the optical and electrical properties of **1** (see below).

The single crystal X-ray diffraction data of **2** reveals a 1D chain structure, crystallizing in the space group of  $P2_1/n$ . The asymmetric unit (Figure 2a) consists of four  $\text{Ag}^+$  ions

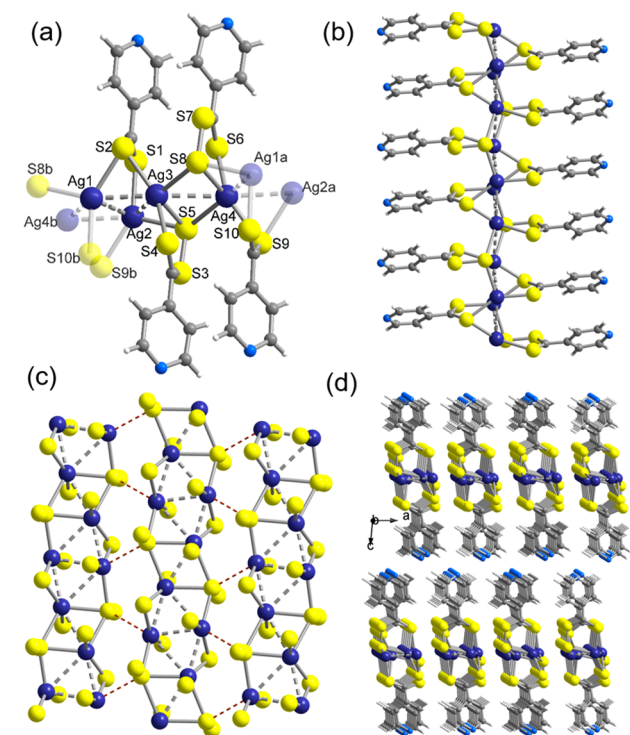


**Figure 2.** Asymmetric unit (a),  $(\text{Ag}_4\text{S}_{10})_\infty$  chain (b), interchain  $\text{Ag}\cdots\text{S}$  interactions (c), and 3D packing diagram (d) of **2**.

coordinated by terminal sulfur atoms from two  $\text{Py-4-CSS}^-$  and two  $\text{Py-4-CSSS}^-$  ligands. Unlike that in **1**, nitrogen atoms of both ligands in **2** do not coordinate to the  $\text{Ag}^+$  ions. The units repeat and form a  $[\text{Ag}_4\text{S}_{10}]_n$  chain along the  $b$  axis (Figure 2b). Intrachain  $\text{Ag-S}$  bond lengths vary from 2.47 to 2.80 Å, while the adjacent  $\text{Ag}\cdots\text{Ag}$  distances vary from 2.89 to 3.30 Å, forming 1D argentophilicity along the chain. The  $[\text{Ag}_4\text{S}_{10}]_n$  chains pack closely along the  $a$  axis, with the shortest interchain  $\text{Ag}\cdots\text{S}$  distance down to 3.00 Å, while the packing along the  $c$  axis is much looser, by only van der Waals forces (Figure 2c,d). IR and Raman spectra also support the existence of perthilcarboxylate groups in **2**. In the IR spectrum of **2** (Figure S12), the major peak at  $1038\text{ cm}^{-1}$  ( $\nu(\text{CS}_2)$ ) is slightly shifted to high energy with respect to the corresponding peak ( $1025\text{ cm}^{-1}$ ) in spectrum of **1**, as repeatedly found for perthiocarboxylates in comparison with the corresponding dithioderivatives.<sup>42</sup> In the Raman (Figure S13), a strong peak at  $466\text{ cm}^{-1}$  indicates the S-S group in **2**.<sup>43</sup>

**Light Absorption.** UV-vis-NIR diffuse reflectance spectra of  $\text{Py-4-CSSNa}$ , **1**, and **2** were measured and transformed into the absorption spectra using the Kubelka-Munk function<sup>44</sup>

(Figure 3). For  $\text{Py-4-CSSNa}$ , there is only one major absorption band before 600 nm and peaking at about 400

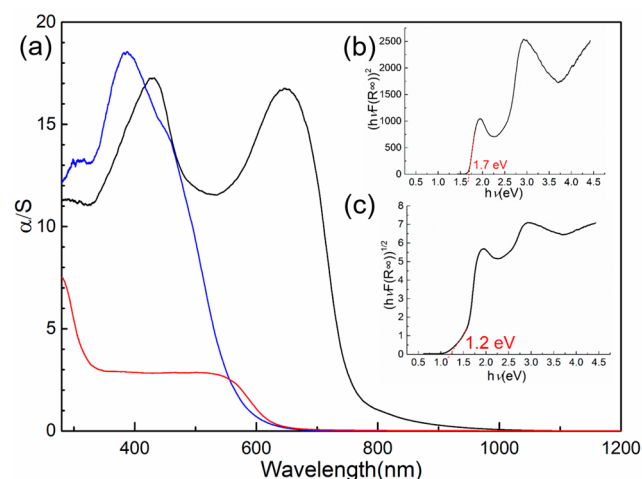


**Figure 3.** Derived absorption spectra of **1** (black), **2** (red), and  $\text{Py-4-CSSNa}$  (blue). Inset: calculated band gaps of **1** for direct (b) and for indirect (c).

nm. While the absorption spectrum of **1** has a second strong peak at ca. 650 nm compared to the  $\text{Py-4-CSSNa}$  compound, indicating the unambiguous effect of coordination with the silver(I) ions. However, there is sharp decrease between 650 and 750 nm, which is intriguingly followed by a long tail until 1000 nm. Though the major absorption lies before 750 nm the wide absorption band between 750 and 1000 nm is in NIR region and indicating a characteristics of narrow band gap semiconductor with possible photothermal effect under NIR radiation. Though compound **2** also shows distinct absorption features compared to the  $\text{Py-4-CSSNa}$ , there is no absorption above 700 nm for **2**, indicating **2** is non-NIR active. Nevertheless, **2** has an optical absorption edge of about 620 nm (2.0 eV), which also falls in the semiconductor region. Compound **1** has an obvious narrower energy gap compared with  $\text{Py-4-CSSNa}$ , compound **2** and some other silver dithiocarboxylate compounds with  $\text{Ag-S}$  chains.<sup>45</sup> It rules out simple reasons, including ligand absorption and quantum confinement effect of  $\text{Ag-S}$  component for the long-wavelength absorption of **1**. In inorganic semiconductors, weak absorption tail indicates an indirect band structure or defect energy levels between bands. Two possible band gaps of **1** can be calculated, respectively, from the optical spectra, giving 1.2 eV for indirect band gap and 1.7 eV for direct band gap. The DFT calculation reveals a direct band structure, but it should be careful to accept a direct band gap of 1.7 eV. In coordination compounds, weak absorption can also be caused by interligand or intraligand charge transfer. The weak absorption of **1** from 750 to 1000 nm may be caused by the enhanced charge transfer from the dithiocarboxylate group to the nitrogen donor of the pyridine ligand, namely,  $\text{CSS} \rightarrow \text{N}$ . Such a charge transfer scheme is presented along with DFT simulated charge density contour plot for **1**. As shown in Figure 4, in the ground state pyridine ligand especially nitrogen donor accumulates larger amount of electron charge than the dithiocarboxylate group. However, the coordinated N is still a stronger electron accepting center,<sup>46</sup> though it has larger Bader charge than other atoms (N:6.35 vs S:6.09  $e$ ). The above-mentioned charge-transfer circumstance is absent in **2** because

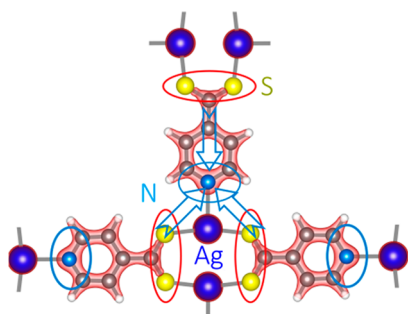


**Figure 4.** DFT calculated real space charge density contour plot and corresponding electron transfer routes in **1** (red circles indicate electron-rich domains; blue circles indicate electron-accepting centers; blue arrows indicate the transfer direction).

the N atoms in both Py-4-CSS and Py-4-CSSS ligands do not coordinate to the silver(I) ions. Moreover, higher dimension of the Ag-CSS-Py network and  $\pi$ - $\pi$  interactions in **1** are also possible favorable factors for the low electron excitation energy.

**Electrical Conductivity.** To reveal the electric conductivity of both compounds two-probe electrical resistivity measurements were carried out on pressed pellets of **1** and **2**. The conductivity of **1** at room temperature is  $1.1 \times 10^{-11}$  S/cm, while that of **2** is  $5.5 \times 10^{-10}$  S/cm (Figure S15), which corroborates that both **1** and **2** are semiconductors.

**Photothermal Effect.** As compound **2** has no absorption in the NIR region, we performed a photothermal measurement only for **1** by measuring the temperature change of a pellet sample under an 800 nm laser radiation of  $0.5 \text{ W cm}^{-2}$ . As shown in Figure 5a, a quick temperature increase ( $12 \text{ }^\circ\text{C}$  in first 15 s) of **1** demonstrates positive photothermal response. Temperature of the sample nearly reach equilibrium within 180 s when the laser was turn off and the maximum temperature difference ( $\Delta T_{\text{max}}$ ) of **1** is  $24.5 \text{ }^\circ\text{C}$ . For comparison, we also tested the photothermal effect of the bulk  $\text{Ag}_2\text{S}$  sample with the same mass (250 mg) and found that both the temperature increasing rate ( $9 \text{ }^\circ\text{C}$  in first 15 s) and  $\Delta T_{\text{max}}$  ( $17.0 \text{ }^\circ\text{C}$ ) are lower than those of **1**.

**Differential Scanning Calorimetry (DSC).** DSC measurements were performed on both samples of **1** and  $\text{Ag}_2\text{S}$  (Figure 5b). In the temperature window of  $20$ – $80 \text{ }^\circ\text{C}$ , the specific heat capacity of **1** is in the scope of  $1.02$ – $1.25 \text{ J/(g}\cdot\text{K)}$ , which is nearly twice the  $\text{Ag}_2\text{S}$  sample (around  $0.7 \text{ J/(g}\cdot\text{K)}$ ).<sup>48</sup> According to the definition of specific heat capacity ( $C_p$ ),

$$C_p = Q/(m \times \Delta T) \quad (1)$$

where  $Q$  is heat (J) and  $m$  is mass (g). As the masses of both samples are the same, the higher  $Q$  is consistent with higher ( $\Delta T_{\text{max}} \times C_p$ ), indicating much more heat was generated in **1** during the irradiation. Thus, in this comparison, **1** shows higher photothermal conversion efficiency than bulk  $\text{Ag}_2\text{S}$ . Though the DSC measurement of **1** indicates exothermic change above  $50 \text{ }^\circ\text{C}$ , TGA plot shows **1** is stable up to  $200 \text{ }^\circ\text{C}$  (Figure S14).

**Photothermal Conversion Efficiency.** With the information on the absorbance, photothermal temperature, and the heat capacity, we can get a coarse photothermal conversion efficiency  $\eta$  of **1** according to the previous method,<sup>49</sup> because

$$mC_p \frac{dT}{dt} = Q_s - Q_{\text{loss}} \quad (2)$$

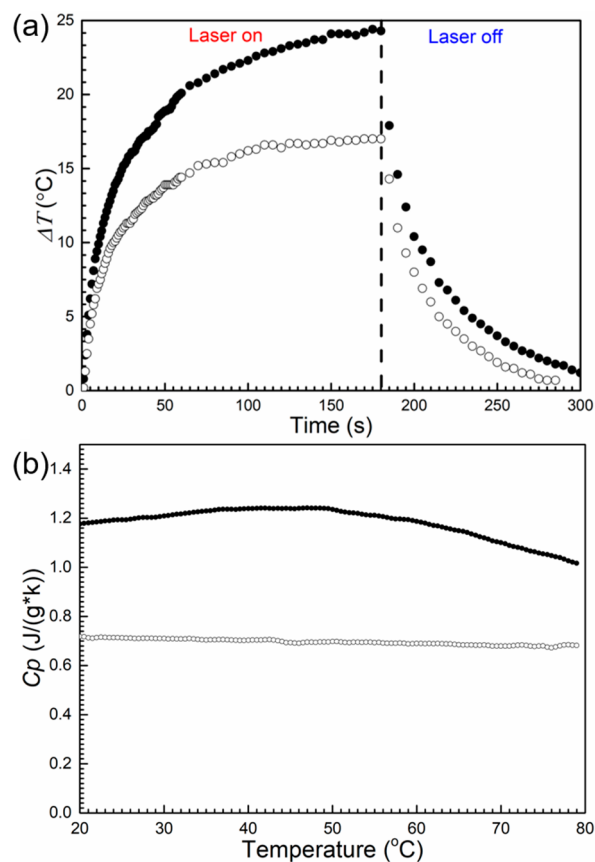


**Figure 5.** Temperature variation of **1** (filled circle) and  $\text{Ag}_2\text{S}$  (empty circle) under the radiation 800 nm laser (a) and temperature-dependent heat capacity of **1** (filled circle) and  $\text{Ag}_2\text{S}$  (empty circle) (b).

where  $m$  and  $C_p$  are the mass and heat capacity of the solid, respectively; while  $Q_s$  is the photothermal heat energy input by irradiating, and

$$Q_s = I(1 - R)\eta \quad (3)$$

where  $I$  is the laser power and  $R$  is the reflectance at the excitation wavelength of 800 nm.  $Q_{\text{loss}}$  is thermal energy lost to the surroundings which is nearly proportional to the linear thermal driving force

$$Q_{\text{loss}} = hS(T - T_{\text{surr}}) \quad (4)$$

where  $h$  is the heat transfer coefficient,  $S$  is the surface area of the container, and  $T_{\text{surr}}$  is the surrounding temperature. When the temperature reaches the maximum, the system is in balance. So,

$$Q_s = Q_{\text{loss}} = hS(T_{\text{max}} - T_{\text{surr}}) \quad (5)$$

For **1**,  $(T_{\text{max}} - T_{\text{surr}})$  is  $24.3 \text{ K}$ . The conversion efficiency  $\eta$  can be deduced according to

$$\eta = \frac{h(T_{\text{max}} - T_{\text{surr}})}{I(1 - R)} \quad (6)$$

In order to get the  $hS$ , a dimensionless driving force  $\theta$  is introduced as follows:

$$\theta = \frac{T - T_{\text{surr}}}{T_{\text{max}} - T_{\text{surr}}} \quad (7)$$

Derive  $\theta$  with respect to  $T$  and substitute the result into eq 2 and we get

$$\frac{d\theta}{dt} = \frac{Q_s}{mC_p(T_{\max} - T_{\text{surr}})} - \frac{hS\theta}{mC_p} \quad (8)$$

When the laser is off,  $Q_s = 0$ , therefore,

$$\frac{d\theta}{dt} = -\frac{hS\theta}{mC_p} \quad (9)$$

And by integration,

$$t = -\frac{mC_p}{hS} \ln \theta \quad (10)$$

So  $hS$  can be calculated from the slope of the plot of cooling time versus  $\ln \theta$  (Figure S10). For **1**,  $hS$  is 0.0067 J/(Ks). According to eq 6, the conversion efficiency  $\eta$  for **1** is finally calculated to be 22.1%, which is among the highest compared to various known inorganic materials (e.g., Au nanoshells (13%), nanorods (21%), and  $\text{Cu}_{2-x}\text{Se}$  nanocrystals (22%) irradiated with 800 nm light.<sup>50</sup>) The photothermal conversion efficiency of the bulk sample of  $\text{Ag}_2\text{S}$  also was calculated to be 9.5% (Figure S11). Under 800 nm irradiation, the absorption ratio ( $1 - \text{reflectance}$ ) of **1** and  $\text{Ag}_2\text{S}$  are 0.737 and 0.947, respectively, which indicates the absorption of **1** is weaker than that of  $\text{Ag}_2\text{S}$ .

There are two major possible directions for the photo-induced electron–hole pairs: radiative recombination for luminescence and nonradiative recombination giving heat. Unlike  $\text{Ag}_2\text{S}$ , known for strong photoluminescence, **1** does not show obvious photoluminescence in our measurement, indicating more light converts into heat.

In theory, nonradiative electron–hole recombination (giving off heat instead of light) requires phonons, and different coordination polymers certainly can have different phonon dispersion and electron–phonon coupling, depending on the exact atomic structure. Electron and hole separated by photon absorption can couple with phonons and form electron polaron and hole polaron. If there is an organic component, the polaronic reconstruction is very conspicuous and fast.<sup>51</sup> While naked electron and naked hole in a normal inorganic band material (like  $\text{Ag}_2\text{S}$ ) can recombine quantum mechanically, to give off light, electron polaron and hole polaron can no longer radiatively recombine, because they are dressed by much heavier phonons (this reduces their energy and is an energy downhill process) and can only move classically. Then, as they are not far apart, they are Coulombically attracted, and it is much easier for electron polaron and hole polaron to just come together and annihilate the charges and disperse the phonons as heat. Here are some basic trends: (a) the higher polarizability, the stronger the trend of polaronic reconstruction; (b) the more flat band (higher electron effective mass), the stronger the trend of polaronic reconstruction; (c) the easier/faster polaronic reconstruction of charge carriers, the more the nonradiative electron–hole recombination compared to radiative recombination. Therefore, the dielectric measurement and calculation of electronic band structure were carried out.

**Dielectric Constant.** At room temperature (25 °C), the dielectric constant in different frequency was determined by measuring the capacitance of a pellet sample of **1**. The dielectric constant of **1** shows obvious frequency dependence. Dielectric constants of **1** in 60, 100, 1000, 10000, and 100000

Hz are 45, 38, 26, 18, and 14 (Figure 6). The values are much higher than 6, known for  $\text{Ag}_2\text{S}$ .

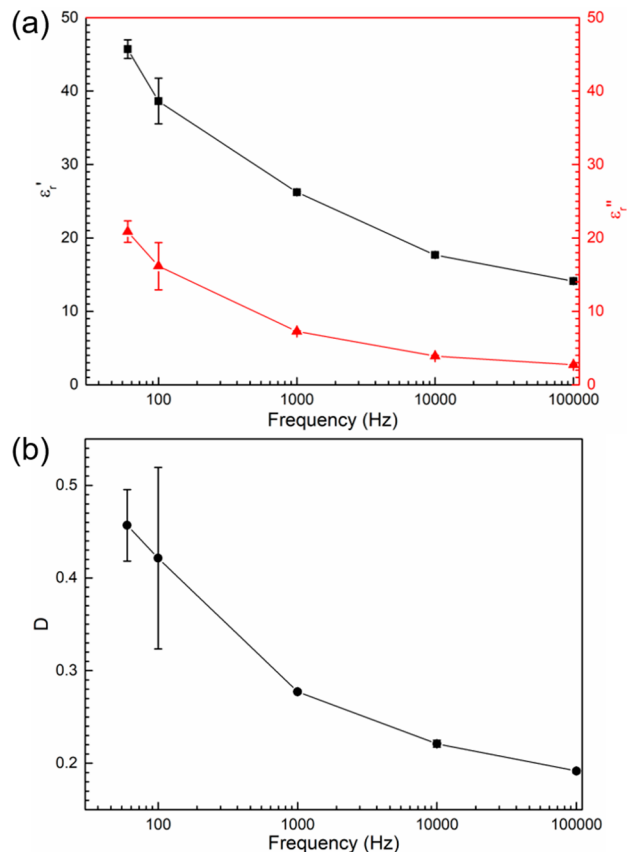


**Figure 6.** Frequency dependence of the real part (black) and imaginary part (red) of dielectric permittivity ( $\epsilon_r'$ ) (a) and the corresponding dielectric loss tangent ( $D$ ) (b) of **1**.

**Electronic Band Structures.** We further investigate the electronic properties of **1** using first-principles calculations, and the comparison between **1** and  $\alpha\text{-Ag}_2\text{S}$  bulk is also presented. We fully optimize the crystal structure for **1**. The comparison between experimental and DFT optimized lattice parameters, bond lengths, and angles of system **1** are summarized in Tables S1 and S2 of the Supporting Information, respectively. The overall good agreements between experimental and simulated results are obtained. Figure 7 displays our calculated energy band structures and PDOS for two compounds.  $\alpha\text{-Ag}_2\text{S}$  is a semiconductor with pronounced hybridization between Ag-5s and S-3p orbitals throughout the entire valence and conduction bands. In **1**, besides Ag–S hybridization, the strong orbital overlap between Ag-5s and N-2p indicates the effective charge transfer within Ag–N bonds. It is noted that we do not found a good match between our calculated and experimentally measured energy band gaps for  $\alpha\text{-Ag}_2\text{S}$  and **1**, owing to the band gap error from GGA exchange–correlation functional.<sup>52</sup> We predict both  $\alpha\text{-Ag}_2\text{S}$  and **1** as direct gap semiconductors, but with distinct energy dispersion features:  $\alpha\text{-Ag}_2\text{S}$  exhibits the strong energy dispersions (1–2 eV) around the valence band maximum and conduction band minimum, while the almost flat valence and conduction bands indicate the high carrier effective mass and poor carrier mobility in **1**.



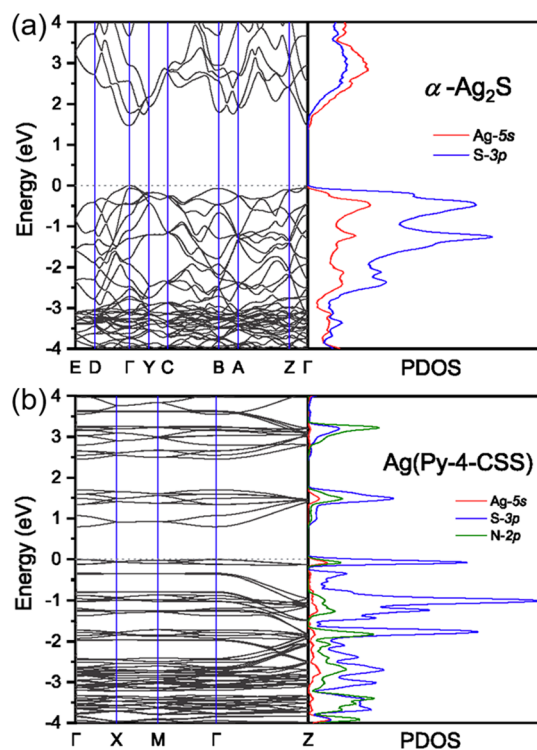


**Figure 7.** Calculated energy band structures and projected density of states (PDOS) for  $\alpha$ -Ag<sub>2</sub>S bulk (a) and **1** (b).

## CONCLUSION

To summarize, we demonstrate a 2D Ag-dithiocarboxylate based CP exhibits stronger NIR photothermal effect compared to the pure inorganic material Ag<sub>2</sub>S. The near-infrared photothermal conversion efficiency of **1** reaches 22.1% in 3 min, which is among the highest compared to various known inorganic materials, for example, Au nanoshells (13%), nanorods (21%), and Cu<sub>2-x</sub>Se nanocrystals (22%). This result shows the inorganic–organic hybrid materials, which can combine high polarity and flat energy band structures are advantageous for efficient photothermal conversion.

## ASSOCIATED CONTENT

### Supporting Information

The Supporting Information is available free of charge on the ACS Publications website at DOI: 10.1021/acs.inorgchem.8b02867.

Crystallographic information files (CIFs) and supporting tables and figures (PDF)

### Accession Codes

CCDC 1819424 and 1821603 contain the supplementary crystallographic data for this paper. These data can be obtained free of charge via [www.ccdc.cam.ac.uk/data\\_request/cif](http://www.ccdc.cam.ac.uk/data_request/cif), or by emailing [data\\_request@ccdc.cam.ac.uk](mailto:data_request@ccdc.cam.ac.uk), or by contacting The Cambridge Crystallographic Data Centre, 12 Union Road, Cambridge CB2 1EZ, U.K.; fax: +44 1223 336033.

## AUTHOR INFORMATION

### Corresponding Authors

\*E-mail: [zheng.yanzhen@xjtu.edu.cn](mailto:zheng.yanzhen@xjtu.edu.cn).

\*E-mail: [gougaoyang@mail.xjtu.edu.cn](mailto:gougaoyang@mail.xjtu.edu.cn).

\*E-mail: [liju@mit.edu](mailto:liju@mit.edu).

## ORCID

Gaoyang Gou: 0000-0003-1485-8115

Ju Li: 0000-0002-7841-8058

Yan-Zhen Zheng: 0000-0003-4056-097X

## Author Contributions

All authors have given approval to the final version of the manuscript.

## Notes

The authors declare no competing financial interest.

## ACKNOWLEDGMENTS

This work was supported by the Natural Science Foundation of China (Nos. 21801202, 21871219, 21620102002, 21773130, and 11574244), State Key Laboratory for Mechanical Behavior of Materials (20182006), Key Laboratory Construction Program of Xi'an Municipal Bureau of Science and Technology (201805056ZD7CG40), the Cyrus Chung Ying Tang Foundation, and the Fundamental Research Funds for the Central Universities.

## REFERENCES

- Gärtner, W. W. Photothermal Effect in Semiconductors. *Phys. Rev.* **1961**, *122*, 419–424.
- Chen, Z.; Wang, Q.; Wang, H.; Zhang, L.; Song, G.; Song, L.; Hu, J.; Wang, H.; Liu, J.; Zhu, M.; Zhao, D. Ultrathin PEGylated W18O49 Nanowires as a New 980 nm-Laser-Driven Photothermal Agent for Efficient Ablation of Cancer Cells In Vivo. *Adv. Mater.* **2013**, *25*, 2095–2100.
- Cheng, L.; Liu, J.; Gu, X.; Gong, H.; Shi, X.; Liu, T.; Wang, C.; Wang, X.; Liu, G.; Xing, H.; Bu, W.; Sun, B.; Liu, Z. PEGylated WS<sub>2</sub> Nanosheets as a Multifunctional Theranostic Agent for in vivo Dual-Modal CT/Photoacoustic Imaging Guided Photothermal Therapy. *Adv. Mater.* **2014**, *26*, 1886–1893.
- Liu, T.; Wang, C.; Gu, X.; Gong, H.; Cheng, L.; Shi, X.; Feng, L.; Sun, B.; Liu, Z. Drug Delivery with PEGylated MoS<sub>2</sub> Nano-sheets for Combined Photothermal and Chemotherapy of Cancer. *Adv. Mater.* **2014**, *26*, 3433–3440.
- Zhou, B.; Li, Y.; Niu, G.; Lan, M.; Jia, Q.; Liang, Q. Near-Infrared Organic Dye-Based Nanoagent for the Photothermal Therapy of Cancer. *ACS Appl. Mater. Interfaces* **2016**, *8*, 29899–29905.
- Yang, K.; Xu, H.; Cheng, L.; Sun, C.; Wang, J.; Liu, Z. In Vitro and In Vivo Near-Infrared Photothermal Therapy of Cancer Using Polypyrrole Organic Nanoparticles. *Adv. Mater.* **2012**, *24*, 5586–5592.
- Zha, Z.; Yue, X.; Ren, Q.; Dai, Z. Uniform Polypyrrole Nanoparticles with High Photothermal Conversion Efficiency for Photothermal Ablation of Cancer Cells. *Adv. Mater.* **2013**, *25*, 777–782.
- Xu, L.; Cheng, L.; Wang, C.; Peng, R.; Liu, Z. Conjugated polymers for photothermal therapy of cancer. *Polym. Chem.* **2014**, *5*, 1573–1580.
- Li, Y.; Lu, W.; Huang, Q.; Li, C.; Chen, W. Copper sulfide nanoparticles for photothermal ablation of tumor cells. *Nanomedicine* **2010**, *5*, 1161–1171.
- Yang, T.; Tang, Y. a.; Liu, L.; Lv, X.; Wang, Q.; Ke, H.; Deng, Y.; Yang, H.; Yang, X.; Liu, G.; Zhao, Y.; Chen, H. Size-Dependent Ag<sub>2</sub>S Nanodots for Second Near-Infrared Fluorescence/Photoacoustics Imaging and Simultaneous Photothermal Therapy. *ACS Nano* **2017**, *11*, 1848–1857.
- Robinson, J. T.; Welsher, K.; Tabakman, S. M.; Sherlock, S. P.; Wang, H.; Luong, R.; Dai, H. High performance in vivo near-IR (>1  $\mu$ m) imaging and photothermal cancer therapy with carbon nanotubes. *Nano Res.* **2010**, *3*, 779–793.
- Yang, J.; Choi, J.; Bang, D.; Kim, E.; Lim, E.-K.; Park, H.; Suh, J.-S.; Lee, K.; Yoo, K.-H.; Kim, E.-K.; Huh, Y.-M.; Haam, S.

Convertible Organic Nanoparticles for Near-Infrared Photothermal Ablation of Cancer Cells. *Angew. Chem., Int. Ed.* **2011**, *50*, 441–444.

(13) Guo, B.; Feng, G.; Manghnani, P. N.; Cai, X.; Liu, J.; Wu, W.; Xu, S.; Cheng, X.; Teh, C.; Liu, B. A Porphyrin-Based Conjugated Polymer for Highly Efficient In Vitro and In Vivo Photothermal Therapy. *Small* **2016**, *12*, 6243–6254.

(14) Yang, Y.; Liu, J.; Liang, C.; Feng, L.; Fu, T.; Dong, Z.; Chao, Y.; Li, Y.; Lu, G.; Chen, M.; Liu, Z. Nanoscale Metal–Organic Particles with Rapid Clearance for Magnetic Resonance Imaging-Guided Photothermal Therapy. *ACS Nano* **2016**, *10*, 2774–2781.

(15) Eddaoudi, M.; Moler, D. B.; Li, H.; Chen, B.; Reineke, T. M.; O’Keeffe, M.; Yaghi, O. M. Modular Chemistry: Secondary Building Units as a Basis for the Design of Highly Porous and Robust Metal–Organic Carboxylate Frameworks. *Acc. Chem. Res.* **2001**, *34*, 319–330.

(16) Yaghi, O. M.; O’Keeffe, M.; Ockwig, N. W.; Chae, H. K.; Eddaoudi, M.; Kim, J. Reticular synthesis and the design of new materials. *Nature* **2003**, *423*, 705.

(17) Kitagawa, S.; Kitaura, R.; Noro, S.-i. Functional Porous Coordination Polymers. *Angew. Chem., Int. Ed.* **2004**, *43*, 2334–2375.

(18) Furukawa, H.; Cordova, K. E.; O’Keeffe, M.; Yaghi, O. M. The Chemistry and Applications of Metal–Organic Frameworks. *Science* **2013**, *341*, 1230444.

(19) Wang, C.; Liu, D.; Lin, W. Metal–Organic Frameworks as a Tunable Platform for Designing Functional Molecular Materials. *J. Am. Chem. Soc.* **2013**, *135*, 13222–13234.

(20) Li, B.; Wang, X.; Chen, L.; Zhou, Y.; Dang, W.; Chang, J.; Wu, C. Ultrathin Cu-TCPP MOF nanosheets: a new theragnostic nanoplatform with magnetic resonance/near-infrared thermal imaging for synergistic phototherapy of cancers. *Theranostics* **2018**, *8*, 4086–4096.

(21) Zhang, Y.; Hong, G.; Zhang, Y.; Chen, G.; Li, F.; Dai, H.; Wang, Q. Ag<sub>2</sub>S Quantum Dot: A Bright and Biocompatible Fluorescent Nanoprobe in the Second Near-Infrared Window. *ACS Nano* **2012**, *6*, 3695–3702.

(22) Kole, G. K.; Vivekananda, K. V.; Kumar, M.; Ganguly, R.; Dey, S.; Jain, V. K. Hemilabile silver(i) complexes containing pyridyl chalcogenolate (S, Se) ligands and their utility as molecular precursors for silver chalcogenides. *CrystEngComm* **2015**, *17*, 4367–4376.

(23) Su, W.; Hong, M.; Weng, J.; Cao, R.; Lu, S. A Semiconducting Lamella Polymer [ $\{\text{Ag}(\text{C}_5\text{H}_4\text{NS})\}_n$ ] with a Graphite-Like Array of Silver(I) Ions and Its Analogue with a Layered Structure. *Angew. Chem., Int. Ed.* **2000**, *39*, 2911–2914.

(24) Xu, Z., Metal–Organic Frameworks: Semiconducting Frameworks. *Encyclopedia of Inorganic and Bioinorganic Chemistry*; John Wiley & Sons, Ltd, 2011.

(25) Kolarik, K.; Sahamies, J.; Kalenius, E.; Novikov, A. S.; Kukushkin, V. Y.; Haukka, M. Metallophilic interactions in polymeric group 11 thiols. *Solid State Sci.* **2016**, *60*, 92–98.

(26) Tang, K.; Jin, X.; Xie, Y.; Tang, Y. Study of tetranuclear Ag cluster compounds. *Chin. J. Nat.* **1984**, *9*, 017.

(27) Tang, K.; Jin, X.; Xie, Y.; Tang, Y. Crystal structure of a tetranuclear silver cluster compounds  $\text{Ag}_4(\alpha\text{-C}_{10}\text{H}_7\text{CS}_2)_4(\text{Py})_4 \cdot 2\text{Py}$ . *Sci. Chin. B* **1986**, *16*, 485–490.

(28) Tang, K.; Jin, X.; Xiao, Q.; Sun, J.; Tang, Y. The Syntheses and Crystal Structures of Tetranuclear Silver Cluster Complex  $\text{Ag}_4(\text{o-CH}_3\text{C}_6\text{H}_4\text{CS}_2)_4(\text{Py})_4$  and Dinuclear Copper Complex  $\text{Cu}_2(\text{o-CH}_3\text{C}_6\text{H}_4\text{CSS}_2)_2(\text{Py})_2$ . *Chin. J. Struct. Chem.* **1988**, *4*, 245–253.

(29) Becke, F.; Hagen, H. Verfahren zur Herstellung von aromatischen Dithiocarbonsauren. DE1274121(B), August 1, 1968.

(30) Coucouvanis, D.; Fackler, J. P. Sulfur Chelates. IV.1 Sulfur Addition to Dithiolato Complexes of Nickel(II). *J. Am. Chem. Soc.* **1967**, *89*, 1346–1351.

(31) Paital, A. R.; Zhan, J.; Kim, R.; Kampf, J.; Collins, P.; Coucouvanis, D. Synthesis and structures of perthio- and polymeric metal complexes with the tetrathio- and dithioterephthalate ligands. *Polyhedron* **2013**, *64*, 328–338.

(32) Sheldrick, G. A short history of SHELX. *Acta Crystallogr., Sect. A: Found. Crystallogr.* **2008**, *64*, 112–122.

(33) Dolomanov, O. V.; Bourhis, L. J.; Gildea, R. J.; Howard, J. A. K.; Puschmann, H. OLEX2: a complete structure solution, refinement and analysis program. *J. Appl. Crystallogr.* **2009**, *42*, 339–341.

(34) Spek, A. PLATON SQUEEZE: a tool for the calculation of the disordered solvent contribution to the calculated structure factors. *Acta Crystallogr., Sect. C: Struct. Chem.* **2015**, *71*, 9–18.

(35) Kresse, G.; Furthmüller, J. Efficient iterative schemes for ab initio total-energy calculations using a plane-wave basis set. *Phys. Rev. B: Condens. Matter Mater. Phys.* **1996**, *54*, 11169–11186.

(36) Kresse, G.; Joubert, D. From ultrasoft pseudopotentials to the projector augmented-wave method. *Phys. Rev. B: Condens. Matter Mater. Phys.* **1999**, *59*, 1758–1775.

(37) Blöchl, P. E. Projector augmented-wave method. *Phys. Rev. B: Condens. Matter Mater. Phys.* **1994**, *50*, 17953–17979.

(38) Sun, J.; Ruzsinszky, A.; Perdew, J. P. Strongly Constrained and Appropriately Normed Semilocal Density Functional. *Phys. Rev. Lett.* **2015**, *115*, 036402.

(39) Tao, J.; Perdew, J. P.; Staroverov, V. N.; Scuseria, G. E. Climbing the Density Functional Ladder: Nonempirical Meta-Generalized Gradient Approximation Designed for Molecules and Solids. *Phys. Rev. Lett.* **2003**, *91*, 146401.

(40) Monkhorst, H. J.; Pack, J. D. Special points for Brillouin-zone integrations. *Phys. Rev. B* **1976**, *13*, 5188–5192.

(41) Che, C.-M.; Tse, M.-C.; Chan, M. C. W.; Cheung, K.-K.; Phillips, D. L.; Leung, K.-H. Spectroscopic Evidence for Argentophilicity in Structurally Characterized Luminescent Binuclear Silver(I) Complexes. *J. Am. Chem. Soc.* **2000**, *122*, 2464–2468.

(42) Manotti Lanfredi, A. M.; Tiripicchio, A.; Marsich, N.; Camus, A. Perthiocarboxylate complex. Synthesis, structure and spectroscopic characterization of the tetrameric copper(I) o-tolylperthiocarboxylate,  $[\text{Cu}(\text{S})\text{SSCC}7\text{H}7]_4$ . *Inorg. Chim. Acta* **1988**, *142*, 269–275.

(43) Marsich, N.; Pellizer, G.; Camus, A.; Manotti Lanfredi, A. M.; Ugozzoli, F. Synthesis and reactivity of the first Ag(I) perthiocarboxylates. Crystal structures of tetra(o-tolylperthiocarboxylato)tetra-silver(I),  $[\text{Ag}_4\text{S}_3\text{C-o-tolyl}]_4$ , and of its cocrystallization product with copper(I),  $[\text{Ag}_1.76\text{Cu}_2.24(\text{S}_3\text{C-o-tolyl})_4]$ . *Inorg. Chim. Acta* **1990**, *169*, 171–179.

(44) Paul, K.; Franz, M. Ein Beitrag zur Optik der Farbanstriche. *Zeitschrift für technische Physik* **1931**, *12*, 593–601.

(45) Manotti Lanfredi, A. M.; Ugozzoli, F.; Camus, A.; Marsich, N. New synthesis and X-ray diffraction study of a polymeric form of Ag(I) dithio-o-toluato,  $[\text{Ag}_4(\text{S}_2\text{C-o-C}_6\text{H}_4\text{CH}_3)_4]_n$ . *J. Chem. Crystallogr.* **1995**, *25*, 37–41.

(46) Vogler, A.; Kunkely, H. Ligand-to-ligand and intraligand charge transfer and their relation to charge transfer interactions in organic zwitterions. *Coord. Chem. Rev.* **2007**, *251*, 577–583.

(47) Givaja, G.; Amo-Ochoa, P.; Gomez-Garcia, C. J.; Zamora, F. Electrical conductive coordination polymers. *Chem. Soc. Rev.* **2012**, *41*, 115–147.

(48) Grønvald, F.; Westrum, E. F. Silver(I) sulfide: Ag<sub>2</sub>S Heat capacity from 5 to 1000 K, thermodynamic properties, and transitions. *J. Chem. Thermodyn.* **1986**, *18*, 381–401.

(49) Kim, B.; Shin, H.; Park, T.; Lim, H.; Kim, E. NIR-Sensitive Poly(3,4-ethylenedioxy-selenophene) Derivatives for Transparent Photo-Thermo-Electric Converters. *Adv. Mater.* **2013**, *25*, 5483–5489.

(50) Hessel, C. M.; Pattani, V. P.; Rasch, M.; Panthani, M. G.; Koo, B.; Tunnell, J. W.; Korgel, B. A. Copper Selenide Nanocrystals for Photothermal Therapy. *Nano Lett.* **2011**, *11*, 2560–2566.

(51) Heeger, A. J.; Kivelson, S.; Schrieffer, J. R.; Su, W. P. Solitons in conducting polymers. *Rev. Mod. Phys.* **1988**, *60*, 781–850.

(52) Baerends, E. J.; Gritsenko, O. V.; van Meer, R. The Kohn–Sham gap, the fundamental gap and the optical gap: the physical meaning of occupied and virtual Kohn–Sham orbital energies. *Phys. Chem. Chem. Phys.* **2013**, *15*, 16408–16425.



## **Supporting Information**

# **Two-Dimensional Silver(I)-Dithiocarboxylate Coordination Polymer Exhibiting Strong Near-Infrared Photothermal Effect**

Mu-Qing Li,<sup>1,2</sup> Min Zhao,<sup>1</sup> Le-Yu Bi,<sup>1</sup> Yue-Qiao Hu,<sup>1,3</sup> Gaoyang Gou,<sup>1,\*</sup> Ju Li<sup>1,4,\*</sup> and Yan-Zhen Zheng<sup>1,\*</sup>

<sup>1</sup> Frontier Institute of Science and Technology (FIST), State Key Laboratory of Mechanical Behavior for Materials, MOE Key Laboratory for Nonequilibrium Synthesis of Condensed Matter, Xi'an Key Laboratory of Sustainable Energy and Materials Chemistry and School of Science, Xi'an Jiaotong University, 99 Yanxiang Road, Xi'an, Shaanxi 710054, P. R. China.

<sup>2</sup> Department of Chemistry, City University of Hong Kong, 83 Tat Chee Avenue, Kowloon, Hong Kong, China

<sup>3</sup> Key Laboratory of Advanced Molecular Engineering Materials, Baoji University of Arts and Sciences, No. 1 Hi-Tec Avenue, Baoji 721013, P. R. China.

<sup>4</sup> Department of Nuclear Science and Engineering, Department of Materials Science and Engineering, Massachusetts Institute of Technology, Cambridge, MA 02139, USA

## Contents

<b>Contents</b> .....	2
<b>Scheme S1.</b> Syntheses of the crystals of <b>1</b> and <b>2</b> .....	4
<b>Figure S1.</b> Single crystals of <b>1</b> .....	4
<b>Figure S2.</b> Single crystals of <b>2</b> .....	4
<b>Figure S3.</b> TEM image of the crystalline <b>1</b> .....	5
<b>Table S1</b> Crystal data and structure refinement for <b>1</b> and <b>2</b> . Simulated results for <b>1</b> are also listed after slash for comparison. ....	5
<b>Table S2</b> Selected bond lengths (Å) and angles (°) for <b>1</b> . Corresponding simulated results of <b>1</b> are also listed in parenthesis for comparison. ....	6
<b>Table S3</b> Selected bond lengths (Å) and angles (°) for <b>2</b> .....	6
<b>Figure S4.</b> $\pi$ - $\pi$ stacking centroid–centroid contact and displacement angle in <b>1</b> .....	7
<b>Figure S5.</b> Powder XRD patterns of <b>1</b> . (a) calculated pattern of <b>1</b> ; (b) experimental pattern of a crystalline sample of <b>1</b> .....	7
<b>Figure S6.</b> Powder XRD patterns of <b>2</b> . (a) calculated pattern of <b>2</b> ; (b) experimental pattern of a crystalline sample of <b>2</b> .....	8
<b>Figure S7.</b> UV-Vis-NIR diffuse reflectance spectra of <b>1</b> (black), <b>2</b> (red), Py-4-CSSNa (blue). ....	8
<b>Figure S8.</b> UV-Vis-NIR diffuse reflectance spectra and the derived absorption spectra of Ag <sub>2</sub> S. ....	9
<b>Figure S9.</b> Tauc plot of Ag <sub>2</sub> S. The direct band gap of Ag <sub>2</sub> S is 1.1 eV.....	9
<b>Figure S10.</b> Cooling time versus $\ln\theta$ of <b>1</b> and linear fit.....	10
<b>Figure S11.</b> Cooling time versus $\ln\theta$ of Ag <sub>2</sub> S and linear fit. ....	10
<b>Figure S12.</b> IR spectra of Py-4-CSSNa(a), <b>1</b> (b) and <b>2</b> (c). ....	11
<b>Figure S13.</b> Raman spectra of <b>1</b> and <b>2</b> .....	11
<b>Figure S14.</b> TGA plots of <b>1</b> (black) and <b>2</b> (red). ....	12
<b>Figure S15.</b> Plots of current density versus electric field strength ( $J$ – $E$ curves) for <b>1</b> (black dots) and <b>2</b> (red dots) at 298 K. ....	12

<b>Figure S16.</b> PXRD patterns of <b>1</b> : (a) calculated; (b) as-made sample and (c) sample stored in air for three days. ....	13
<b>Figure S17.</b> IR spectra of <b>1</b> : (a) as-made sample and (b) sample stored in air for three days. ....	13
<b>Figure S18.</b> PXRD patterns of <b>2</b> : (a) calculated; (b) as-made sample and (c) sample stored in air for three days. ....	14
<b>Figure S19.</b> IR spectra of <b>2</b> : (a) as-made sample and (b) sample stored in air for three days. ....	14
<b>Figure S20.</b> NMR spectra of Py-4-CSSNa (a), <b>1</b> -extract2 from Na <sub>2</sub> S treatment (b) and <b>2</b> -extract2 from Na <sub>2</sub> S treatment (c). ....	15



**Scheme S1.** Syntheses of the crystals of **1** and **2**

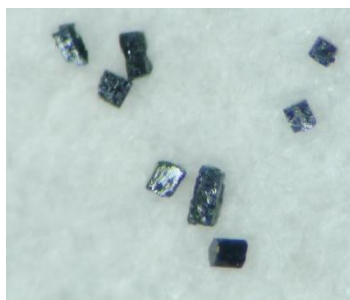
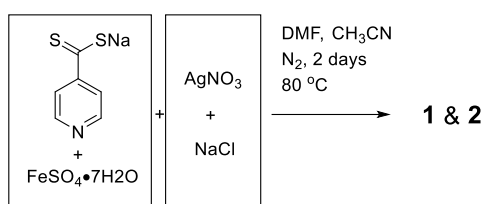


**Figure S1.** Single crystals of **1**

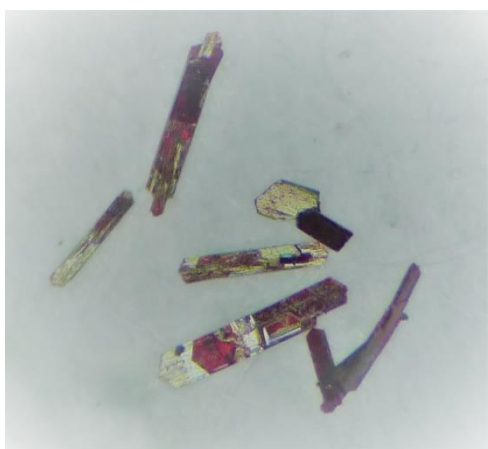


**Figure S2.** Single crystals of **2**.

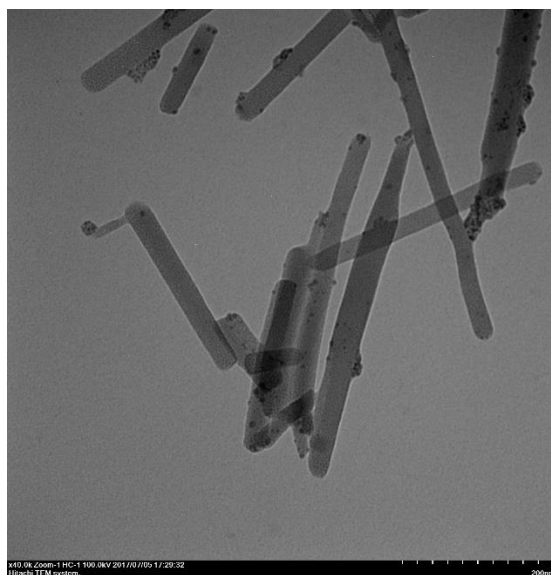


**Figure S3.** TEM image of the crystalline **1**.

**Table S1** Crystal data and structure refinement for **1** and **2**. Simulated results for **1** are also listed after slash for comparison.

	<b>1</b>	<b>2</b>
<b>Empirical formula</b>	C <sub>24</sub> H <sub>16</sub> Ag <sub>4</sub> N <sub>4</sub> S <sub>8</sub>	C <sub>24</sub> H <sub>16</sub> Ag <sub>4</sub> N <sub>4</sub> S <sub>10</sub>
<b>Formula weight</b>	1048.37	1112.49
<b>Temperature/K</b>	296.15	296.15
<b>Crystal system</b>	tetragonal	monoclinic
<b>Space group</b>	<i>P4/ncc</i>	<i>P2<sub>1</sub>/n</i>
<b><i>a</i>/Å</b>	16.125(3)/ 16.0111	11.861(5)
<b><i>b</i>/Å</b>	16.125(3)/ 16.0111	7.723(3)
<b><i>c</i>/Å</b>	7.2075(12)/ 7.0950	33.601(15)
<b><i>α</i>/°</b>	90/ 90	90
<b><i>β</i>/°</b>	90/ 90	95.299(5)
<b><i>γ</i>/°</b>	90/ 90	90
<b><i>V</i>/Å<sup>3</sup></b>	1874.1(8)/ 1818.83	3065(2)
<b><i>Z</i></b>	2	4
<b><math>\rho_{\text{calc}}</math> / g cm<sup>-3</sup></b>	1.858	2.411
<b><math>\mu</math>/mm<sup>-1</sup></b>	2.525	3.227
<b><i>F</i>(000)</b>	1008.0	2144.0
<b>Reflections collected</b>	8244	24415
<b><i>R</i><sub>int</sub></b>	0.0259	0.0664
<b>Data/ parameters</b>	1220/48	5302/379
<b>GOF</b>	1.022	1.113
<b><i>R</i><sub>1</sub>, <i>wR</i><sub>2</sub> [<i>I</i> &gt; 2σ(<i>I</i>)]</b>	0.0306, 0.0744	0.0626, 0.1113
<b><i>R</i><sub>1</sub>, <i>wR</i><sub>2</sub> (all data)</b>	0.0418, 0.0787	0.1103, 0.1238

**Table S2** Selected bond lengths (Å) and angles (°) for **1**. Corresponding simulated results of **1** are also listed in parenthesis for comparison.

bond	length (Å)	angle	angle degree (°)
Ag1-Ag1 <sup>a</sup>	3.0439(9) (3.0546)	S1-Ag1-Ag1 <sup>a</sup>	85.359(18) (83.87)
Ag1-S1 <sup>b</sup>	2.4259(8) (2.4190)	S1 <sup>b</sup> -Ag1-Ag1 <sup>a</sup>	85.359(18) (83.87)
Ag1-S1	2.4259(7) (2.4190)	S1-Ag1-S1 <sup>b</sup>	170.72(4) (167.75)
Ag1-N1 <sup>c</sup>	2.531(3) (2.4747)	S1-Ag1-N1 <sup>c</sup>	94.641(18) (96.13)
Ag1 <sup>d</sup> -N1	2.530(3) (2.4747)	S1 <sup>b</sup> -Ag1-N1 <sup>c</sup>	94.641(18) (96.13)
		N1 <sup>c</sup> -Ag1-Ag1 <sup>a</sup>	180.000(14) (180.00)
<sup>a</sup> 1/2-X,3/2-Y,+Z; <sup>b</sup> 1-Y,1-X,1/2-Z; <sup>c</sup> 1/2-Y,1+X,+Z; <sup>d</sup> -1+Y,1/2-X,+Z			

**Table S3** Selected bond lengths (Å) and angles (°) for **2**.

bond	length (Å)	angle	angle degree (°)	angle	angle degree (°)	angle	angle degree (°)	angle	angle degree (°)
Ag3-Ag4	3.0152(16)	Ag4-Ag3-Ag2	104.21(5)	S8-Ag4-Ag3	58.42(7)	S2-Ag1-Ag2	86.08(8)	S1-Ag2-S9 <sup>b</sup>	147.68(12)
Ag3-Ag1	2.8865(18)	Ag1-Ag3-Ag4	161.96(5)	S8-Ag4-Ag1 <sup>a</sup>	50.62(7)	S2-Ag1-S8 <sup>b</sup>	108.42(11)	Ag1-S2-Ag3	68.73(9)
Ag3-Ag2	3.2985(19)	Ag1-Ag3-Ag2	57.87(4)	S8-Ag4-Ag2 <sup>a</sup>	106.33(8)	S8 <sup>b</sup> -Ag1-Ag3	162.24(8)	Ag4-S8-Ag3	66.59(8)
Ag3-S2	2.562(3)	S2-Ag3-Ag4	123.74(8)	S8-Ag4-S5	113.40(10)	S8 <sup>b</sup> -Ag1-Ag4 <sup>b</sup>	53.47(8)	Ag1 <sup>a</sup> -S8-Ag3	134.18(13)
Ag3-S8	2.799(3)	S2-Ag3-Ag1	55.46(8)	S5-Ag4-Ag3	54.98(7)	S8 <sup>b</sup> -Ag1-Ag2	105.44(8)	Ag1 <sup>a</sup> -S8-Ag4	75.92(9)
Ag3-S5	2.689(3)	S2-Ag3-Ag2	80.12(8)	S5-Ag4-Ag1 <sup>a</sup>	152.25(7)	S10 <sup>b</sup> -Ag1-Ag3	91.11(9)	S7-S8-Ag3	111.25(16)
Ag3-S4	2.589(4)	S2-Ag3-S8	95.51(10)	S5-Ag4-Ag2 <sup>a</sup>	139.56(8)	S10 <sup>b</sup> -Ag1-Ag4 <sup>b</sup>	85.67(8)	S7-S8-Ag4	102.93(15)
Ag4-Ag1 <sup>a</sup>	3.2486(18)	S2-Ag3-S5	121.45(10)	S9-Ag4-Ag3	124.56(8)	S10 <sup>b</sup> -Ag1-Ag2	86.72(9)	S7-S8-Ag1 <sup>a</sup>	101.79(16)
Ag4-Ag2 <sup>a</sup>	2.8866(18)	S2-Ag3-S4	150.68(11)	S9-Ag4-Ag1 <sup>a</sup>	80.84(8)	S10 <sup>b</sup> -Ag1-S2	146.32(12)	Ag3-S5-Ag4	66.68(8)
Ag4-S8	2.691(4)	S8-Ag3-Ag4	54.99(7)	S9-Ag4-Ag2 <sup>a</sup>	55.21(8)	S10 <sup>b</sup> -Ag1-S8 <sup>b</sup>	105.22(11)	Ag2-S5-Ag3	77.10(9)
Ag4-S5	2.795(3)	S8-Ag3-Ag1	140.35(8)	S9-Ag4-S8	122.61(10)	Ag4 <sup>b</sup> -Ag2-Ag3	120.96(5)	Ag2-S5-Ag4	134.89(13)
Ag4-S9	2.551(3)	S8-Ag3-Ag2	151.54(8)	S9-Ag4-S5	95.40(10)	Ag4 <sup>b</sup> -Ag2-Ag1	66.77(4)	S3-S5-Ag3	103.01(15)
Ag4-S6	2.573(3)	S5-Ag3-Ag4	58.34(7)	S9-Ag4-S6	148.93(11)	Ag1-Ag2-Ag3	54.19(4)	S3-S5-Ag4	111.31(15)
Ag1-Ag4 <sup>b</sup>	3.2486(18)	S5-Ag3-Ag1	105.41(8)	S6-Ag4-Ag3	82.20(8)	S5-Ag2-Ag3	52.62(8)	S3-S5-Ag2	102.07(15)
Ag1-Ag2	3.0141(18)	S5-Ag3-Ag2	50.29(7)	S6-Ag4-Ag1 <sup>a</sup>	109.52(8)	S5-Ag2-Ag4 <sup>b</sup>	160.64(8)	Ag2 <sup>a</sup> -S9-Ag4	69.12(9)
Ag1-S2	2.552(3)	S5-Ag3-S8	113.33(10)	S6-Ag4-Ag2 <sup>a</sup>	104.22(9)	S5-Ag2-Ag1	104.11(8)		
Ag1-S8 <sup>2</sup>	2.589(3)	S4-Ag3-Ag4	81.49(9)	S6-Ag4-S8	83.39(10)	S9 <sup>b</sup> -Ag2-Ag3	115.18(8)		
Ag1-S10 <sup>b</sup>	2.467(4)	S4-Ag3-Ag1	105.64(9)	S6-Ag4-S5	87.88(10)	S9 <sup>b</sup> -Ag2-Ag4 <sup>b</sup>	55.67(8)		
Ag2-Ag4 <sup>b</sup>	2.8866(18)	S4-Ag3-Ag2	110.12(9)	Ag3-Ag1-Ag2	122.67(5)	S9 <sup>b</sup> -Ag2-Ag1	85.88(8)		
Ag2-S5	2.603(3)	S4-Ag3-S8	87.46(11)	Ag3-Ag1-Ag2	67.93(4)	S9 <sup>b</sup> -Ag2-S5	108.16(11)		
Ag2-S9 <sup>b</sup>	2.538(3)	S4-Ag3-S5	83.20(10)	Ag2-Ag1-Ag4 <sup>b</sup>	54.74(4)	S1-Ag2-Ag3	85.29(9)		
Ag2-S1	2.465(4)	Ag3-Ag4-Ag1 <sup>a</sup>	104.77(5)	S2-Ag1-Ag3	55.80(8)	S1-Ag2-Ag4 <sup>b</sup>	92.70(10)		
S3-S5	2.025(4)	Ag2 <sup>a</sup> -Ag4-Ag3	163.17(5)	S2-Ag1-Ag4 <sup>b</sup>	116.00(8)	S1-Ag2-Ag1	87.11(9)		
S7-S8	2.027(5)	Ag2 <sup>a</sup> -Ag4-Ag1 <sup>a</sup>	58.50(4)	S2-Ag1-Ag2	86.08(8)	S1-Ag2-S5	104.15(12)		
<sup>a</sup> +X,1+Y,+Z; <sup>b</sup> +X,-1+Y,+Z									



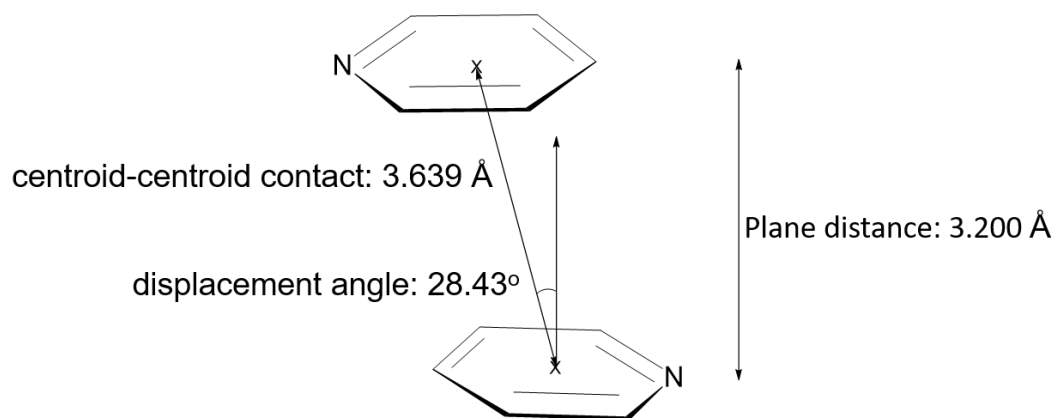


**Figure S4.**  $\pi$ - $\pi$  stacking centroid-centroid contact and displacement angle in **1**.

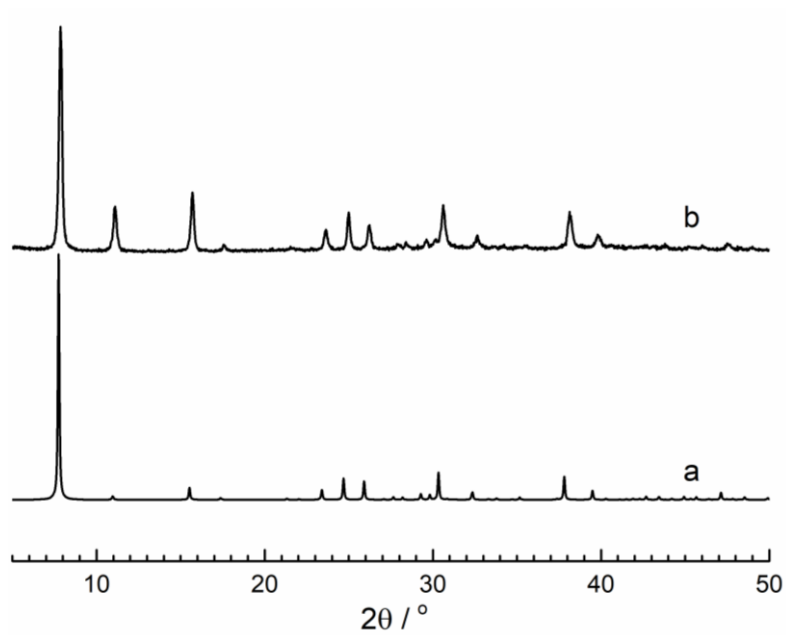


**Figure S5.** Powder XRD patterns of **1**. (a) calculated pattern of **1**; (b) experimental pattern of a crystalline sample of **1**.

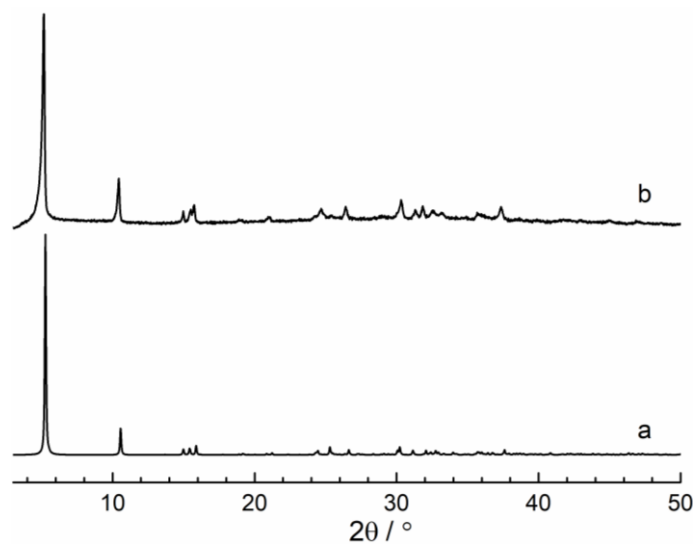


**Figure S6.** Powder XRD patterns of **2**. (a) calculated pattern of **2**; (b) experimental pattern of a crystalline sample of **2**.

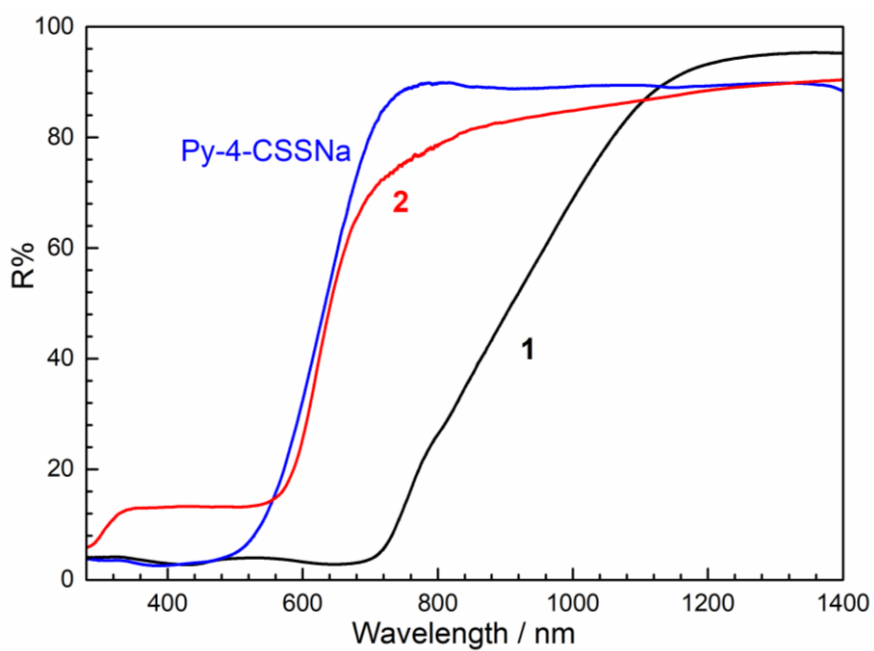


**Figure S7.** UV-Vis-NIR diffuse reflectance spectra of **1** (black), **2** (red), Py-4-CSSNa (blue).

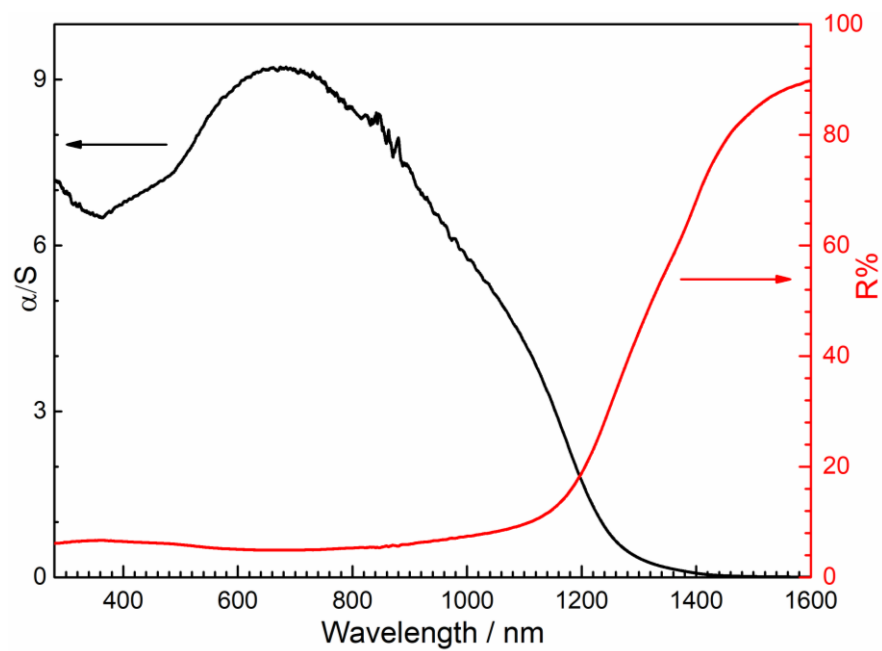


**Figure S8.** UV-Vis-NIR diffuse reflectance spectra and the derived absorption spectra of  $\text{Ag}_2\text{S}$ .

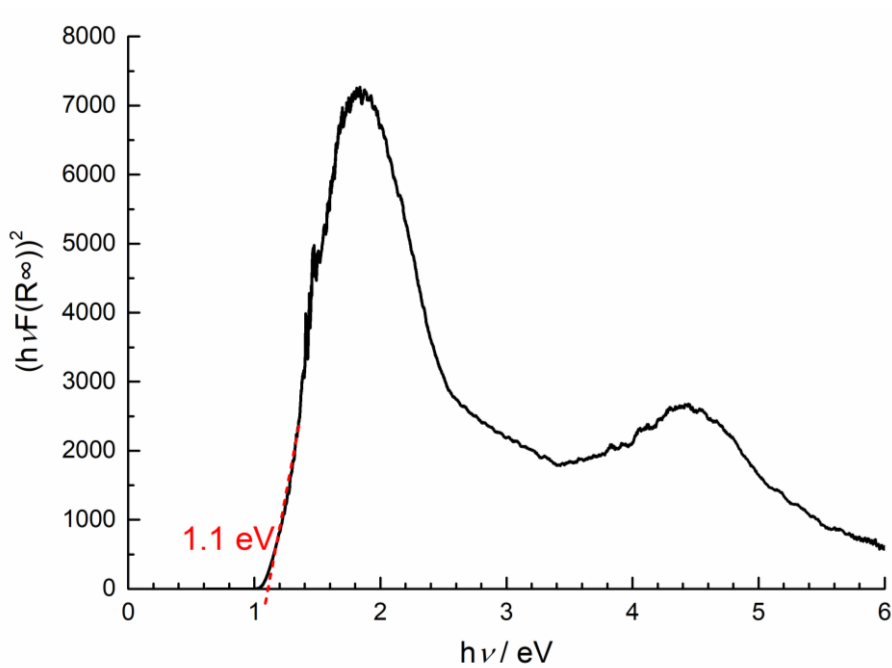


**Figure S9.** Tauc plot of  $\text{Ag}_2\text{S}$ . The direct band gap of  $\text{Ag}_2\text{S}$  is 1.1 eV.



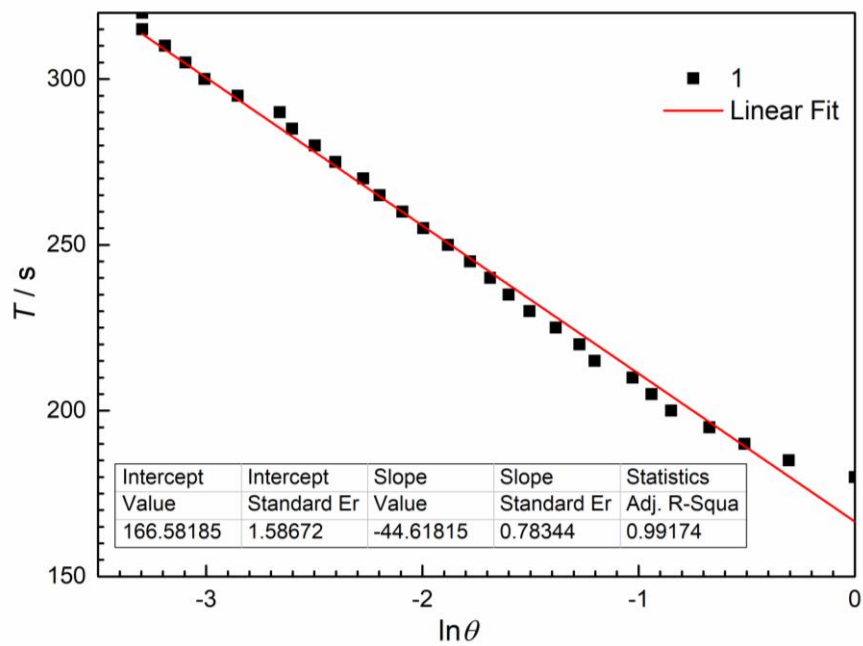


**Figure S10.** Cooling time versus  $\ln\theta$  of **1** and linear fit.

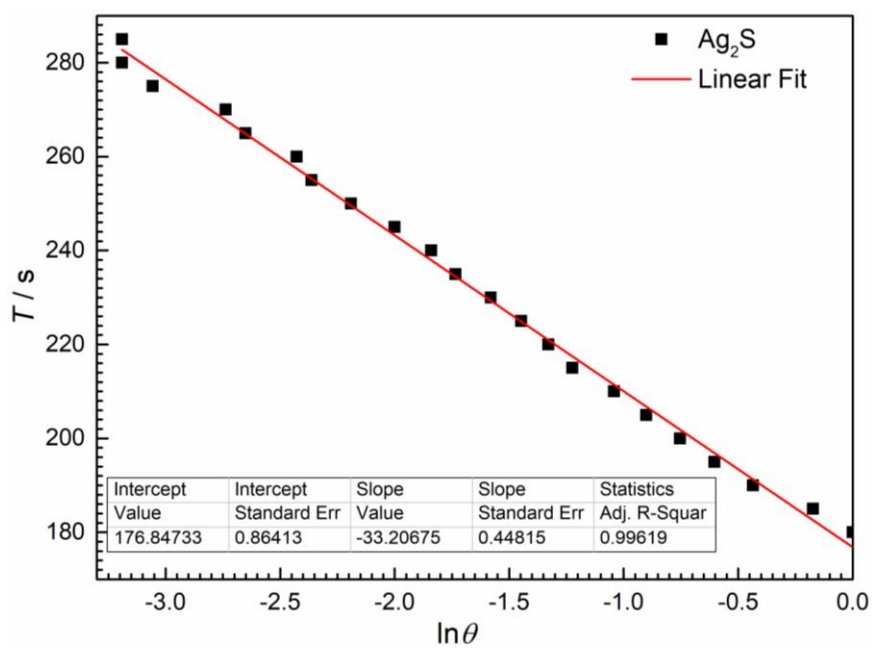


**Figure S11.** Cooling time versus  $\ln\theta$  of **Ag<sub>2</sub>S** and linear fit.

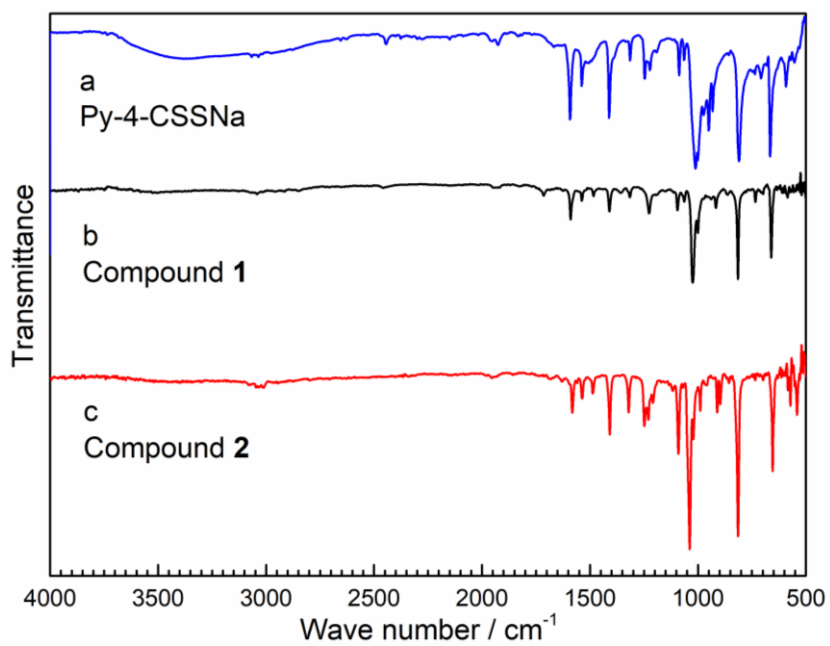


**Figure S12.** IR spectra of Py-4-CSSNa(a), **1** (b) and **2** (c).

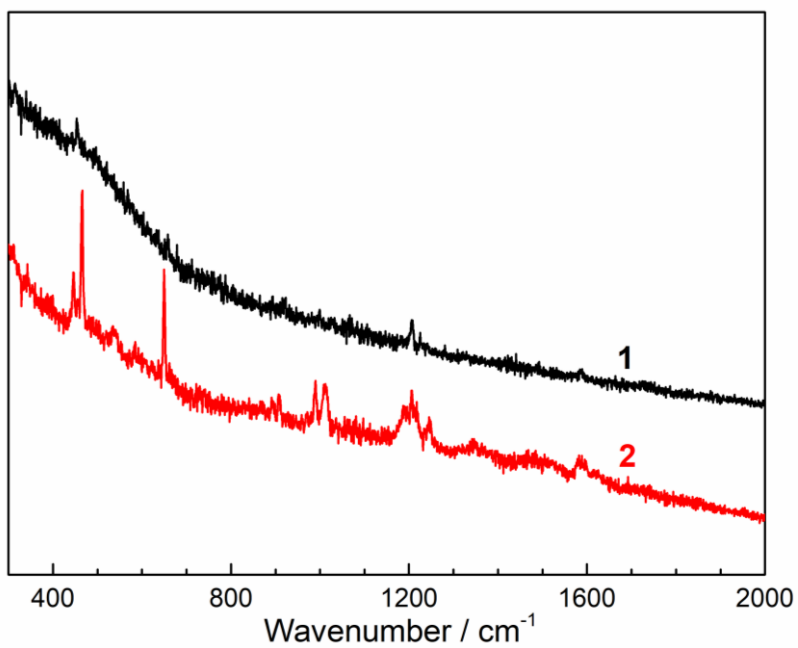


**Figure S13.** Raman spectra of **1** and **2**.

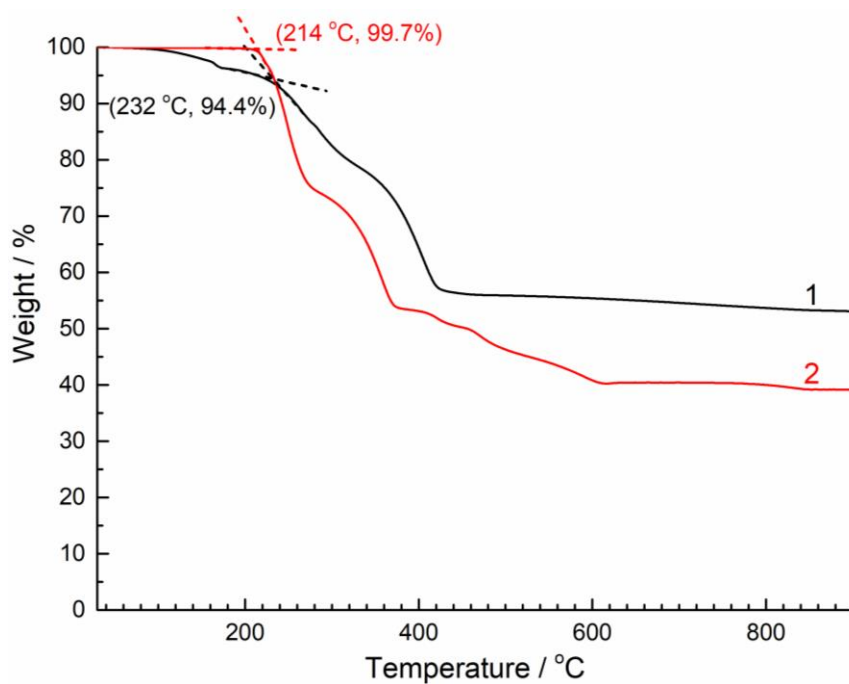


**Figure S14.** TGA plots of **1** (black) and **2** (red).

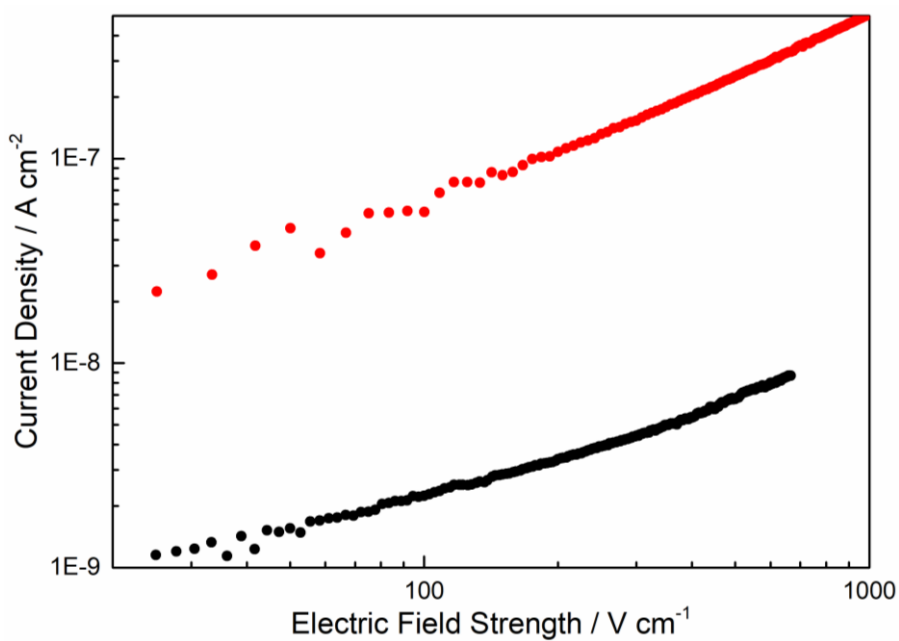


**Figure S15.** Plots of current density versus electric field strength ( $J$ - $E$  curves) for **1** (black dots) and **2** (red dots) at 298 K.

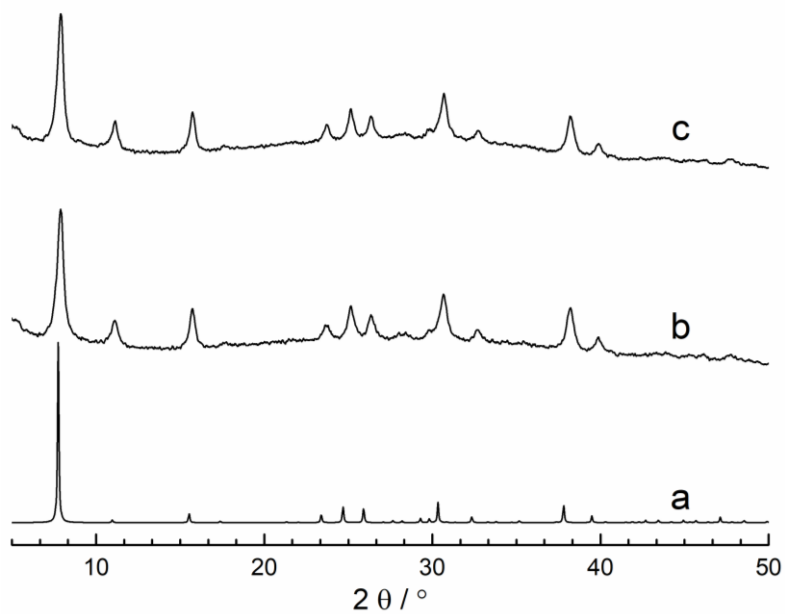


**Figure S16.** PXRD patterns of **1**: (a) calculated; (b) as-made sample and (c) sample stored in air for three days.

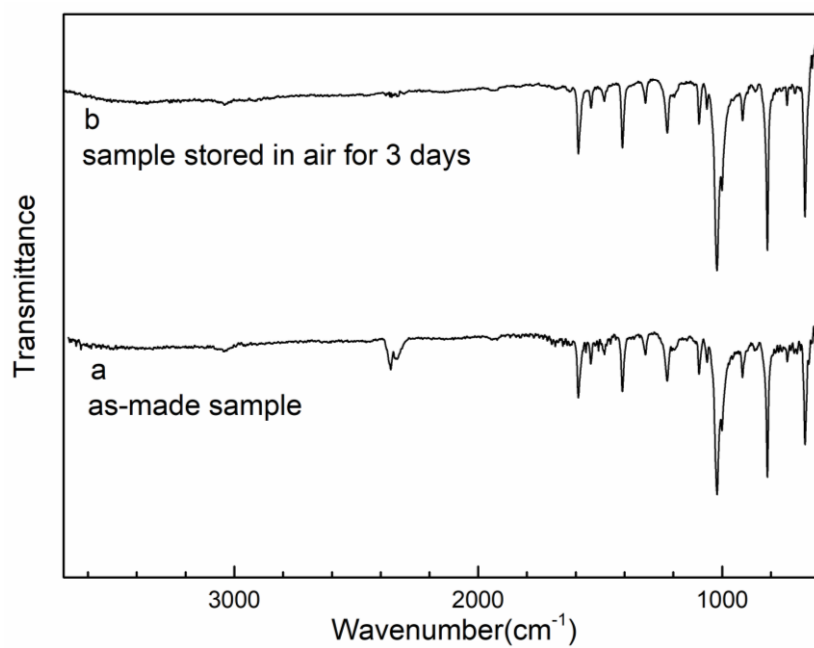


**Figure S17.** IR spectra of **1**: (a) as-made sample and (b) sample stored in air for three days.

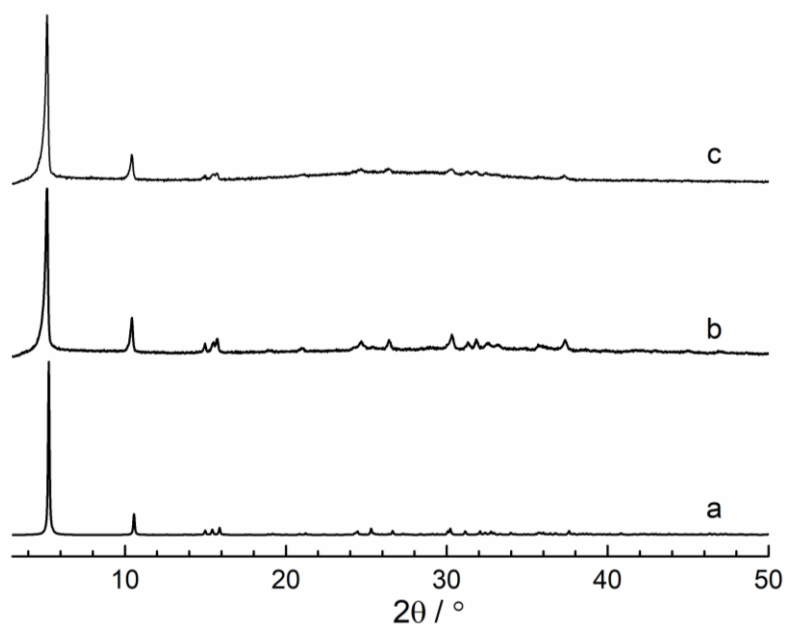


**Figure S18.** PXRD patterns of **2**: (a) calculated; (b) as-made sample and (c) sample stored in air for three days.

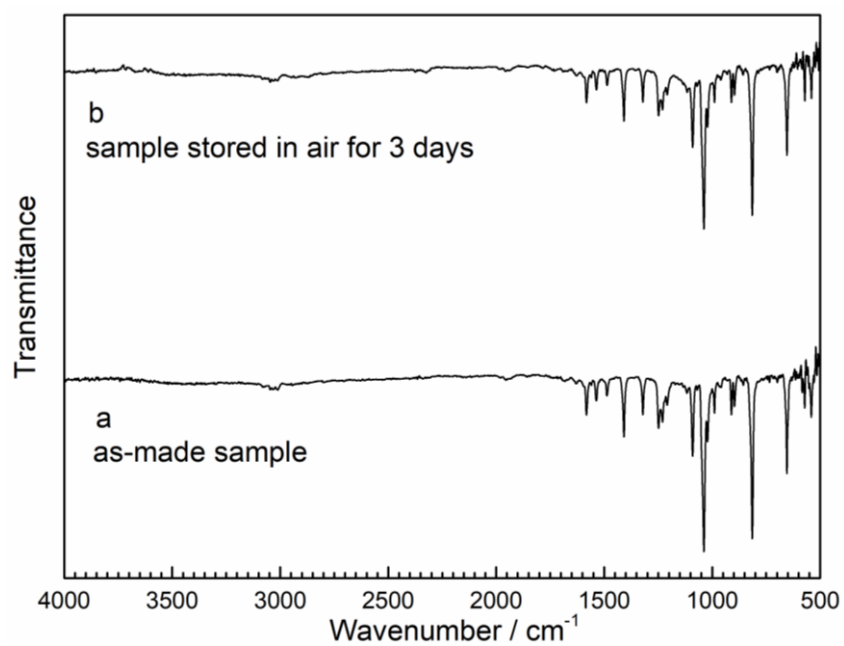


**Figure S19.** IR spectra of **2**: (a) as-made sample and (b) sample stored in air for three days.



### Na<sub>2</sub>S treatment of 1 and 2.

Na<sub>2</sub>S (50 mg), a sample of **1** or **2** (20 mg) and methanol (2 mL) were mixed in a glass vial with stir for 30 minutes. The suspension was then filtered and the filtrate (i.e. **1**-extract1 or **2**-extract1) was used for mass spectroscopy. Pieces with  $m/z=154.08$  were found in both samples, indicating existence of Py-4-CSS<sup>-</sup>. However, the pieces of Py-4-CSSS<sup>-</sup> (calculated  $m/z=185.95$ ) were not found in **2**-extract1, indicating the ligand is not stable in such a treatment.

Na<sub>2</sub>S (50 mg), a sample of **1** or **2** (20 mg) and methanol-d<sub>4</sub> (0.6 mL) were mixed in a glass vial with stir for 30 minutes. The suspension was then filtered and the filtrate (i.e. **1**-extract2 or **2**-extract2) was used for NMR analysis. The NMR spectrum of **2**-extract2 is the same with that of Py-4-CSSNa and **1**-extract2 (Figure S20), which also indicated the instability of Py-4-CSSS<sup>-</sup> in the Na<sub>2</sub>S treatment.

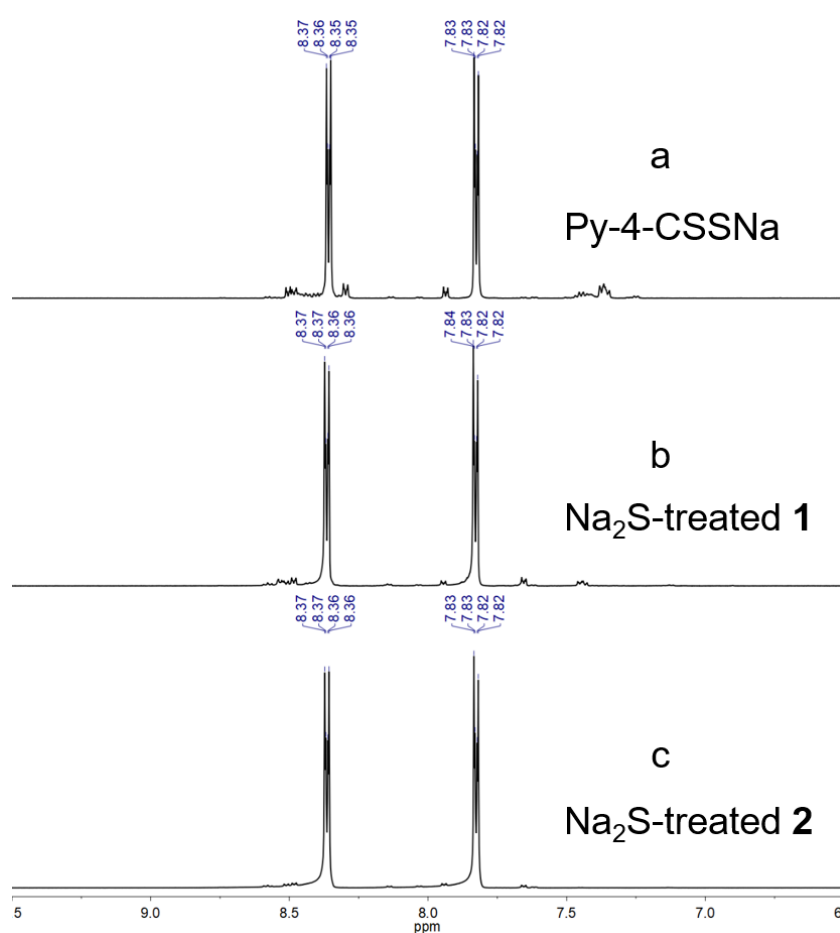


**Figure S20.** NMR spectra of Py-4-CSSNa (a), **1**-extract2 from Na<sub>2</sub>S treatment (b) and **2**-extract2 from Na<sub>2</sub>S treatment (c).